Article

Cell Stem Cell

Self-Organizing 3D Human Trunk Neuromuscular Organoids

Graphical Abstract

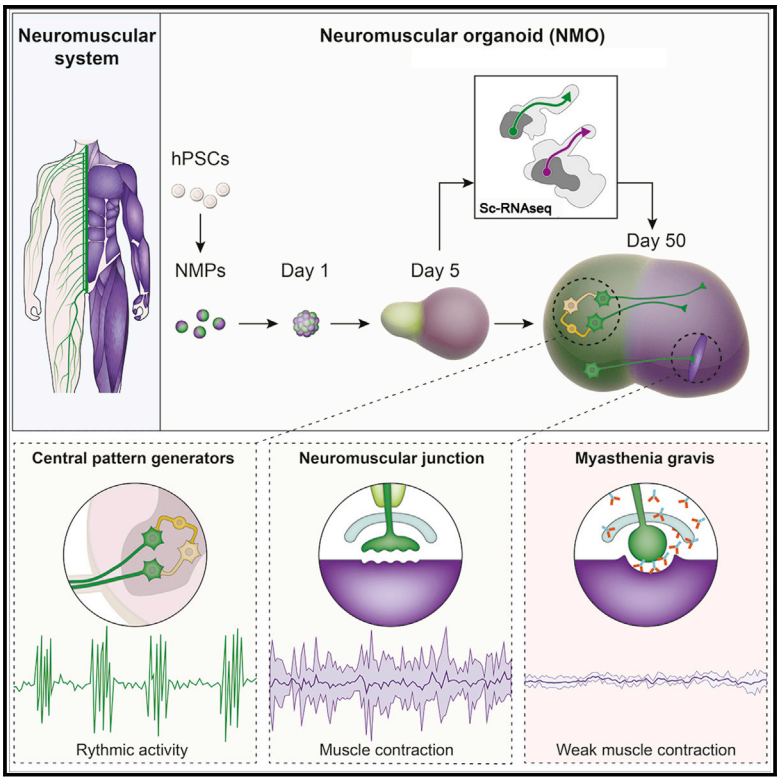

Authors

Jorge-Miguel Faustino Martins, Cornelius Fischer, Alessia Urzi, ..., Simone Spuler, Sascha Sauer, Mina Gouti

Correspondence

mina.gouti@mdc-berlin.de

In Brief

Neuromesodermal progenitors, also known as axial stem cells, are important for the generation of the posterior part of the body. Faustino Martins et al. demonstrate that hPSC-derived neuromesodermal progenitors generate human neuromuscular organoids in 3D culture that form functional neuromuscular junctions and can be used to model neuromuscular diseases.

Highlights

- hPSC-derived neuromesodermal progenitors generate functional NMOs in 3D
- Functional NMJs are generated in NMOs supported by terminal Schwann cells
- NMOs contract and develop central pattern generator-like circuits
- NMOs can be used to model key aspects of myasthenia gravis

Faustino Martins et al., 2020, Cell Stem Cell *26*, 1–15
February 6, 2020
https://doi.org/10.1016/j.stem.2019.12.007

CellPress

Please cite this article in press as: Faustino Martins et al., Self-Organizing 3D Human Trunk Neuromuscular Organoids, Cell Stem Cell (2019), https://doi.org/10.1016/j.stem.2019.12.007

Cell Stem Cell
Article

Self-Organizing 3D Human Trunk Neuromuscular Organoids

Jorge-Miguel Faustino Martins,[1] Cornelius Fischer,[2] Alessia Urzi,[1] Ramon Vidal,[2] Severine Kunz,[4] Pierre-Louis Ruffault,[3] Loreen Kabuss,[1] Iris Hube,[1] Elisabeta Gazzerro,[5] Carmen Birchmeier,[3] Simone Spuler,[5] Sascha Sauer,[2] and Mina Gouti[1,6,*]

[1]Stem Cell Modelling of Development & Disease Group, Max Delbrück Center for Molecular Medicine, 13125 Berlin, Germany
[2]Scientific Genomics Platforms, Laboratory of Functional Genomics, Nutrigenomics and Systems Biology, Max Delbrück Center for Molecular Medicine, 13125 Berlin, Germany
[3]Developmental Biology and Signal Transduction Group, Max Delbrück Center for Molecular Medicine, 13125 Berlin, Germany
[4]Electron Microscopy Core Facility, Max Delbrück Center for Molecular Medicine, 13125 Berlin, Germany
[5]Muscle Research Unit, Experimental and Clinical Research Center (ECRC), Charité Medical Faculty, and Max Delbrück Center for Molecular Medicine, 13125 Berlin, Germany
[6]Lead Contact
*Correspondence: mina.gouti@mdc-berlin.de
https://doi.org/10.1016/j.stem.2019.12.007

SUMMARY

Neuromuscular networks assemble during early human embryonic development and are essential for the control of body movement. Previous neuromuscular junction modeling efforts using human pluripotent stem cells (hPSCs) generated either spinal cord neurons or skeletal muscles in monolayer culture. Here, we use hPSC-derived axial stem cells, the building blocks of the posterior body, to simultaneously generate spinal cord neurons and skeletal muscle cells that self-organize to generate human neuromuscular organoids (NMOs) that can be maintained in 3D for several months. Single-cell RNA-sequencing of individual organoids revealed reproducibility across experiments and enabled the tracking of the neural and mesodermal differentiation trajectories as organoids developed and matured. NMOs contain functional neuromuscular junctions supported by terminal Schwann cells. They contract and develop central pattern generator-like neuronal circuits. Finally, we successfully use NMOs to recapitulate key aspects of myasthenia gravis pathology, thus highlighting the significant potential of NMOs for modeling neuromuscular diseases in the future.

INTRODUCTION

Three-dimensional (3D), self-organizing, *in vitro* tissue models called organoids have been developed for a range of human tissues, including the retina, brain, spinal cord, intestine, kidney, liver, and pancreas (Broutier et al., 2016; Eiraku and Sasai, 2012; Huch et al., 2015; Lancaster et al., 2013; Morizane et al., 2015; Paşca et al., 2015; Spence et al., 2011). Cellular interactions in a 3D space are important for achieving better self-organization of tissue architecture; therefore, 3D organoids are generally considered a promising approach for tissue and disease modeling (Brassard and Lutolf, 2019) and were used successfully to model human diseases in which a single, specific tissue is affected (Rowe and Daley, 2019). However, the study of diseases affecting a process in which more than a single tissue participates, such as neuromuscular disorders, remains a challenge. Neuromuscular diseases are caused by functional defects of the nervous system or skeletal muscle, or arise by defects of the neuromuscular junction (NMJ) (Sanes and Lichtman, 1999). The NMJ is a highly organized chemical synapse formed between motor neurons (MNs) and skeletal muscles and it contains an additional important cell type, the terminal Schwann cells. In some of these disorders, only the muscle or the neural components are initially affected, but in many cases, it is difficult to identify the primary cause and cell type affected. In addition, some diseases exhibit regional specificity. Prominent examples are a group of >30 different acquired and genetic diseases characterized by neuromuscular transmission defects. Many of these diseases are incompletely understood and have no treatment. In addition, muscular dystrophies as well as MN diseases can have secondary effects at the NMJ, and they have mostly escaped experimental approaches (Engel, 2018; Nicolau et al., 2019). Thus, it becomes apparent that generation of all NMJ components with precise positional identity from human pluripotent stem cells (hPSCs) in a 3D organoid system that also possesses positional identity becomes a necessity to study the mechanisms of specific neuromuscular disorders. Significant progress has been made in the generation of either spinal cord neurons or skeletal muscles in 2D culture systems (Chal et al., 2015, 2016; Gouti et al., 2014; Lippmann et al., 2015; Maury et al., 2015; Sances et al., 2016) and the development of 2D and 3D co-culture systems (Afshar Bakooshli et al., 2019; Machado et al., 2019; Maffioletti et al., 2018; Osaki et al., 2018; Santhanam et al., 2018; Steinbeck et al., 2016). However, no study has thus far succeeded in simultaneously generating all of the components of the NMJ, including terminal Schwann cells, that are essential for the maturation and support of NMJs (Darabid et al., 2014). Here, we report a complex 3D organoid model in which all components of the NMJs are generated from the same progenitor population, self-organize, and form functional NMJs.

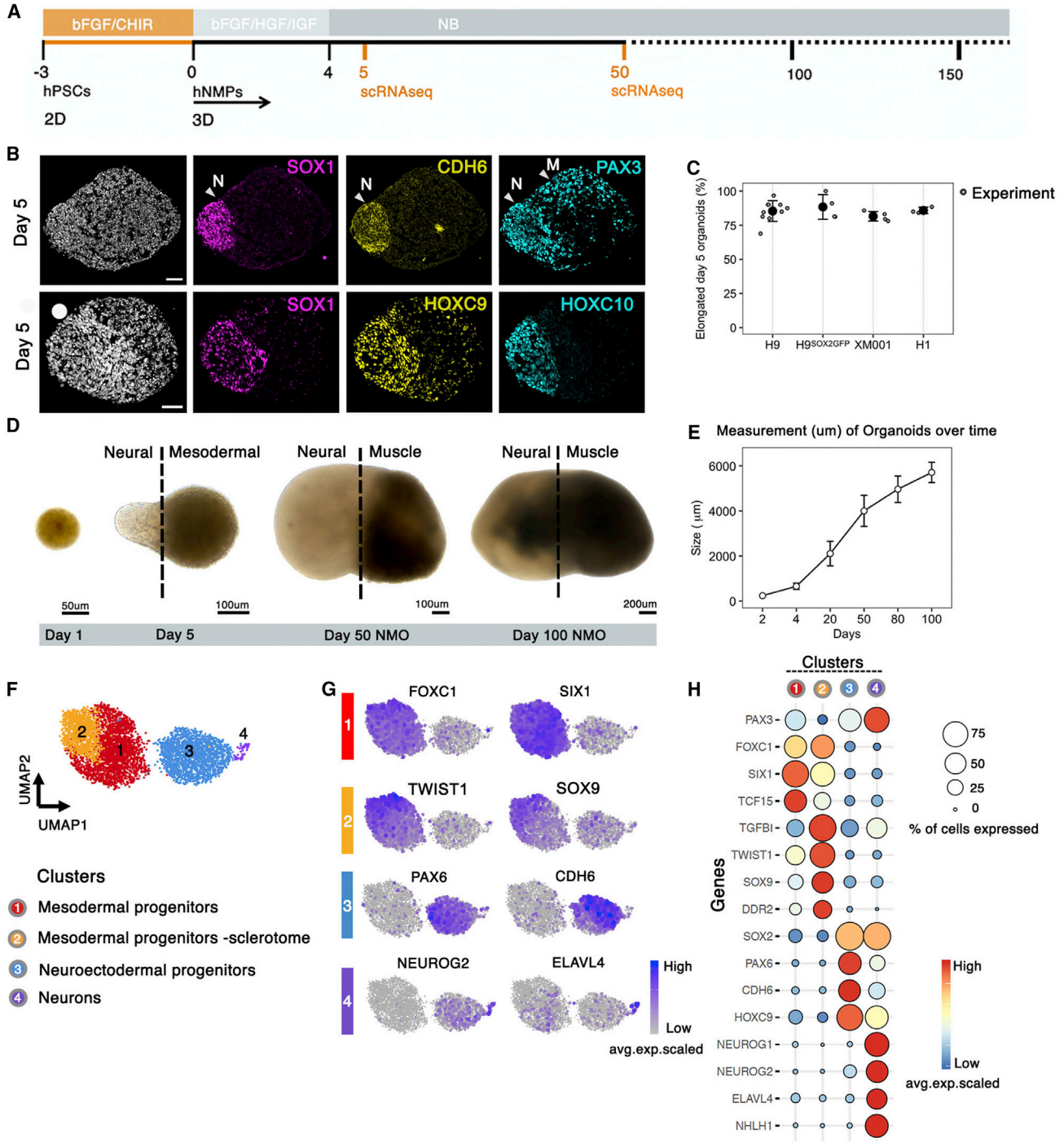

Figure 1. Generation of Human Self-Organizing NMOs in 3D from NMPs

(A) Schematic representation of the strategy used to generate NMOs from hPSCs.

(B) Immunofluorescence analysis of sectioned organoids at day 5 showing the expression of the neural progenitor marker SOX1 and CDH6 in a polarized region of the organoid. PAX3^{+} cells are located in the SOX1^{+} region but also in the SOX1^{-} mesodermal region. Arrows indicate the neural (N) and mesodermal (M) regions of the organoid. The posterior identity of the organoid is determined by the expression of HOXC9 and HOXC10.

(C) Percentage of elongated organoids at day 5 of NMO development in different hPSC lines (H9, H9^{SOX2GFP}, XM001, and H1) (n = 1,145, N = 21). The number of organoids analyzed (n) and the number of experiments (N) from each cell line are summarized in Table S1.

(D) Bright-field images of representative organoids at different stages (days 1, 5, 50, and 100).

(E) Graph showing the growth (average diameter) of NMOs during different development stages.

(F) UMAP projection and determined clusters of day 5 organoids reveals 4 main populations.

(G) UMAP plots showing gene expression levels of representative signature genes for each cluster; related to Table S2.

(legend continued on next page)

To achieve this, we followed the logic of applying the early embryonic developmental principles in a human 3D *in vitro* model. A number of recent studies have established the common developmental origin of the spinal cord and associated musculoskeletal system from a bipotent axial stem cell population called neuromesodermal progenitors (NMPs) (Gouti et al., 2017; Henrique et al., 2015; Metzis et al., 2018; Tzouanacou et al., 2009; Wilson et al., 2009). NMPs reside in the node-streak border of elongating embryos and are important for axial elongation and formation of the spinal cord and musculoskeletal system (Cambray and Wilson, 2002; Henrique et al., 2015; Wilson et al., 2009). NMPs have been identified in the posterior epiblast of all vertebrate species examined, from fish to humans, indicating that they represent a conserved axial stem cell population during development (Kimelman, 2016; Olivera-Martinez et al., 2012). However, their potential to generate these tissues in an *in vitro* 3D human organoid system remains unexplored.

Here, we used hPSC-derived NMPs, the building blocks of the posterior body (Frith et al., 2018; Gouti et al., 2014, 2017; Lippmann et al., 2015; Verrier et al., 2018), to recapitulate the simultaneous development of the spinal cord neural and mesodermal lineages in complex, 3D organoids. The two lineages interact as they develop and, during their maturation, they self-organize to form functional NMJs comprising spinal cord neurons, skeletal muscles, and terminal Schwann cells. The neuromuscular organoids (NMOs) acquire a posterior axial identity, develop contractile activity driven by functional NMJs, are electrophysiologically active, and form central pattern generator (CPG)-like circuits. Our data show that the NMOs represent a complex model system that is highly reproducible across experiments and different hPSC lines and is amenable to functional testing and manipulation. They can be maintained as 3D structures for several months while the component tissues mature, giving unprecedented access to human developmental events and allowing analysis of the specific contributions of different cell types to neuromuscular disorders. Finally, we used NMOs to model myasthenia gravis (MG), an autoimmune disorder that selectively targets the NMJ. Treatment of the NMOs with autoantibodies from MG patient serum resulted in severe defects of the integrity of the NMJs and reduced contractile activity of the muscle, which represent key features of the disease pathology.

RESULTS

Self-Organization of hPSC-Derived NMP Cells in 3D

We used hPSCs (H9 and H1 human PSC lines, and the XM001 induced PSC [iPSC] line) to generate NMPs by recapitulating the early embryonic developmental events *in vitro* (Frith et al., 2018; Gouti et al., 2014; Lippmann et al., 2015; Verrier et al., 2018). We reasoned that NMPs would be the appropriate starting population for the generation of NMOs as they are bipotent and fated to form both neuroectodermal and mesodermal cell derivatives without generating the endodermal derivatives. In addition, they are primed to develop exclusively into tissues of the posterior body (Deschamps and Duboule, 2017; Gouti et al., 2017; Metzis et al., 2018). Initial exposure of hPSCs to Wnt and fibroblast growth factor (FGF) signals for 3 days resulted in the efficient generation of human NMP cells characterized by the co-expression of the neural progenitor marker SOX2, the nascent mesodermal marker Brachyury (T/BRA), and the posterior determinant CDX2 (Figures S1A–S1E) (Frith et al., 2018; Gouti et al., 2014; Verrier et al., 2018). NMP cells were then induced to form 3D aggregates on round-bottomed ultra-low-adhesion 96-well plates in neurobasal (NB) medium supplemented with growth factors (FGF/hepatocyte growth factor [HGF]/insulin-like growth factor [IGF]) (Figure 1A), which enhanced the expansion of mesodermal progenitors during the first days of culture (Chal and Pourquié, 2017). Initially, the aggregates formed round structures, transiently containing NMP cells, which underwent morphogenetic movements during days 0–5 (Video S1). The initial movement resulted in the segregation of a clear region corresponding to neuroectoderm, as evidenced by SOX1 and localized cadherin-6 (CDH6) expression, and a mesodermal region expressing PAX3 but not SOX1 (Figure 1B). The posterior identity was confirmed by the strong expression of HOXC9 in the neural part of the developing organoid and HOXC10 expression in the polarized tip (Figure 1B) (Deschamps and Duboule, 2017; Forlani et al., 2003). To assess the reproducibility of the system, comparing different organoids, experiments (batches), and different cell lines, we quantified the number of organoids that showed the characteristic elongated pattern at day 5 in 4 different hPSC lines (H9, H9^{SOX2GFP}, H1, and XM001) and at least 3 different experiments. More than 80% of the organoids had the characteristic elongated morphology, independent of cell line, clone, or batch (Figures 1C and 1D; Table S1). The organoids grew rapidly until day 50, when they reached a mean core size of 4–5 mm in diameter. Their growth continued but slowed, and they reached an average of 6 mm in diameter at day 100 (Figures 1D and 1E). Notably, these organoids can survive for prolonged periods (currently 1 year in culture) without obvious signs of deterioration.

To determine the major cell populations at the early stages of organoid formation and to assess their differentiation potential, we analyzed the transcriptomes of 5,135 cells from day 5 organoids (H9 line) using microdroplet-based single-cell RNA sequencing. On average, we determined 11,840 unique reads, accounting for 3,333 genes, per cell. The application of a non-linear dimensionality reduction visualization algorithm, uniform manifold approximation, and projection (Becht et al., 2018) to all single cells resulted in the identification of 4 clusters at day 5 (Figure 1F). The main separation was between 2 mesodermal (clusters 1 and 2) and 2 neural clusters (clusters 3 and 4). The cells in clusters 1 and 2 were expressing genes such as *FOXC1* and *SIX1*, characteristic of the developing paraxial mesoderm and somite; cluster 2 cells expressed additional genes such as *TGFBI*, *TWIST1*, and *SOX9* typical of the developing ventral somite and sclerotome (Figures 1G and 1H). The cells in cluster 3 were expressing genes associated with the

(H) Dot plot showing the expression of representative genes across the 4 main clusters. The size of each circle reflects the percentage of cells in a cluster where the gene is detected, and the color reflects the average expression level within each cluster (blue, low expression; red, high expression).
Data are represented as mean ± SD.
See also Table S1.

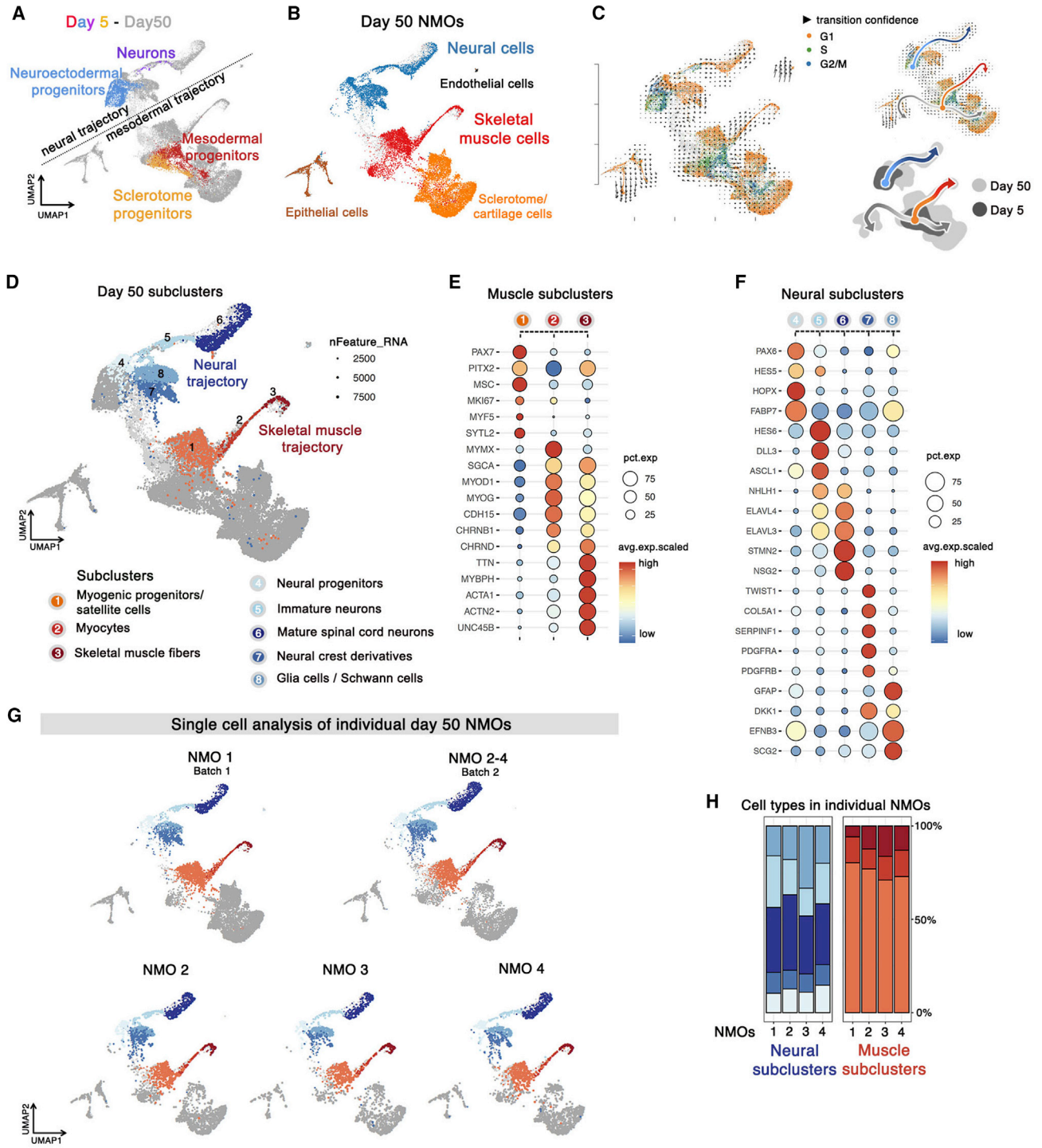

Figure 2. Single-Cell Analysis of Days 5–50 Developmental Trajectories and Cellular Composition of Day 50 NMOs

(A) UMAP plot of integrated days 5 and 50 datasets. The 4 main cell clusters at day 5 are colored, whereas day 50 cells are gray. Dots represent individual cells and colors indicate cluster identity. Related to Table S2.

(B) UMAP plot of the day 50 NMO cells revealed 5 main cell clusters. Dots represent individual cells, and colors indicate cluster identity.

(C) Velocity field overlaid with the UMAP plot showing the developmental trajectories that days 5 and 50 cells follow. Colors indicate the different cell-cycle phases: G1, orange; S, green; and G2-M, blue. The main developmental trajectories are shown with colored arrows: blue for the neural lineage and red for the skeletal muscle lineage. Density plot of day 5 (dark gray) and day 50 (light gray) single cells with colored arrows show the main developmental trajectories that single cells follow as they commit to specific lineages.

(legend continued on next page)

neuroectodermal lineage such as *PAX6*, *SOX2*, and *CDH6*, whereas the few cells of cluster 4 were already committed to a more differentiated state expressing neural specific genes such as *NEUROG1*, *NEUROG2*, *NHLH1*, and *ELAVL4* (Figures 1G and 1H; Table S2). In all 4 clusters, posterior *HOX* genes were upregulated, while anterior genes such as *FOXG1*, *OTX1*, *DLX2*, *DLX5*, and *SIX3* were not detected, further confirming the posterior identity of these organoids (Figure S3A). To further evaluate the reproducibility of the day 5 organoids at the cellular level, we used cell hashing to analyze 2 different organoid populations (Stoeckius et al., 2018). The distribution of the cells and different clusters were strikingly similar in the 2 samples (Figure S1F). The analysis at day 5 revealed that the major populations, normally derived from NMPs in the developing embryo, were now generated from human NMPs *in vitro* in 3D organoids (Gouti et al., 2017).

Self-Organization of Spinal Cord MNs and Skeletal Muscles in NMOs

To examine the potential of these organoids to self-organize and generate spinal cord neurons and skeletal muscles, we maintained them for prolonged periods in 3D using minimal media conditions (NB) and analyzed them at different time points. Analysis at day 10 revealed the presence of OLIG2$^+$ ventral spinal cord progenitor cells (Figure S2A) and co-expression of the trunk neural crest markers SOX9, SOX10, and HOXC9 (Figure S1G). At day 20, the expression of OLIG2 was downregulated, concomitant with the differentiation of MN progenitors to numerous ISLET1$^+$ MNs (Figures S2B and S2C). However, the myogenic progenitor markers MYOD/DESMIN were specifically expressed in the mesodermal part of the organoid (Figures S2D and S2E). The presence of both MNs and myoblasts at that stage suggested that the organoids were maturing over time following the *in vivo* sequence of events.

At day 50, NMOs retained the characteristic morphology whereby the neural and muscle regions could be clearly distinguished by bright-field imaging (Figure 1D). To examine the full repertoire of cells generated during organoid development, we performed single-cell RNA sequencing of 4 individual organoids (total cells 17,294) at day 50. Uniform manifold approximation and projection (UMAP) of days 5 and 50 single cells from corresponding organoids revealed 2 major differentiation routes, 1 associated with a neural differentiation trajectory and 1 associated with a mesodermal differentiation trajectory (Figures 2A and 2B; Table S2). UMAP analysis of day 50 NMOs suggested the presence of 5 broad cell populations (Figure 2B), 1 neural population (blue), and 4 mesodermal-derived populations corresponding to skeletal muscle (red), epithelial (brown), endothelial (black), and sclerotome/cartilage (orange) cells (Figures 2A and 2B; Table S2). Cell-cycle analysis of single cells as they transit from day 5 to day 50 revealed that most day 5 cells were in S and G2/M phases, while day 50 cells were mostly in G1 phase (Figure 2C). These results were consistent with the ongoing maturation of the NMOs.

To identify distinct cell populations at day 50 NMOs, we focused on the skeletal muscle- and neural-specific trajectories. RNA velocity unveiled the dynamics and directionality of differentiation trajectories (Figure 2C) (La Manno et al., 2018). In the skeletal muscle trajectory, day 5 mesodermal progenitors gave rise to myogenic progenitor/satellite-like cells (cluster 1, Figure 2D) which then differentiated through myocytes (cluster 2, Figure 2D) to contractile skeletal muscle cells (cluster 3, Figures 2D, and 2E). The first signs of muscle maturation appeared after 40–50 days in culture, as it was then that the NMOs began contracting in 3D (Video S2), suggesting the formation of functional networks between spinal cord neurons and skeletal muscles. In the neural trajectory, day 5 neuroectodermal progenitors gave rise to neural progenitors (cluster 4, Figure 2D), which differentiated through immature neurons (cluster 5, Figure 2D) into mature spinal cord neurons (cluster 6, Figure 2D). In addition, day 5 neuroectodermal cells gave rise to trunk neural crest derivatives (cluster 7, Figure 2D) as well as glia and Schwann cells (cluster 8, Figures 2D, and 2F).

To determine whether the different populations were reproducibly generated in different NMOs and batches, we clustered all of the cells of the individual batches and aligned them with the cell populations found in individual NMOs (Figure 2G). The data show that the cellular composition and developmental trajectories are reproducibly established in each organoid (Figures 2G and 2H). The expression of cell-type-specific neural and muscle markers assayed by immunohistochemistry further confirmed the high consistency among individual organoids at the protein level (Figures S4A–S4C).

Organization and Maturation of Trunk NMOs

The separation of the neural and muscle compartments observed in early NMOs was also maintained at day 50, with clear evidence of extensive neuromuscular interactions. Skeletal muscle fibers were localized in a well-defined region of the organoid that was expressing myosin skeletal fast (Fast MyHC), whereas the neural part was enriched for TUJ1$^+$ neurons that were also innervating the muscle region (Figures 3A and 3B). Axonal tracts innervating the skeletal muscle were clearly evident by the expression of the mature neurofilament marker SMI32 in the muscle compartment (Figure S4E). To assess the reproducibility of the organoids, we analyzed the percentage of neural and muscle populations in at least 3 individual organoids from 3 different batches in 3 different hPSC lines (H9, H1, and

(D) Sub-clustering of the neural and skeletal muscle trajectories reveals 8 additional clusters. Shades of blue and red show the different neural and muscle subclusters, respectively. Related to Table S2.

(E and F) Dot plot showing the expression of representative genes across the 3 subclusters present in the skeletal muscle trajectory (E) and across the 5 subclusters present in the neural differentiation trajectory (F). The size of each circle reflects the percentage of cells in a cluster where the gene is detected, and the color intensity reflects the average expression level within each cluster (blue: low expression, red: high expression).

(G) To access the reproducibility of gene expression patterns in organoids, single-cell sequencing was performed on 4 individual day 50 NMOs from 2 different batches of the H9 hPSC line. UMAP analysis of each organoid shows that all of the different populations are reproducibly generated.

(H) Percentage of cells from each individual organoid belonging to each cell subcluster in identically processed datasets from day 50 NMOs (2 batches, n = 4 individual organoids).

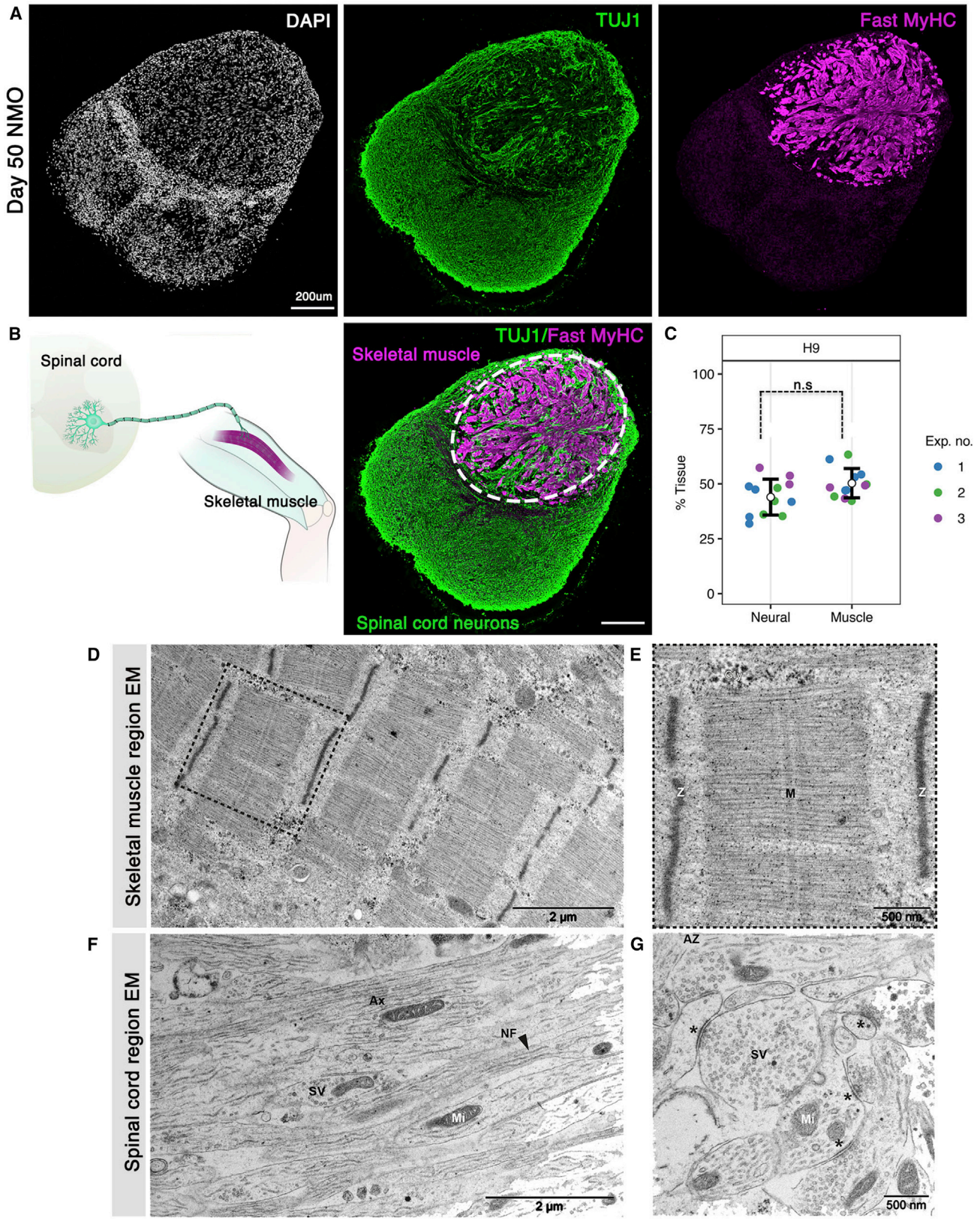

(legend on next page)

XM001 hPSCs). The data suggested that NMOs of any given hPSC line reproducibly organize into muscle and neural regions with similar proportions between different batches (Figures 3C and S4A–S4D). In agreement with a predisposition of different human PSC lines to favor differentiation into specific germ layers (Osafune et al., 2008), we observed that while the H9 hPSC line was generating muscle and neural tissue in roughly equal proportions, the H1 and XM001 PSC lines had a slight preference for muscle and neural tissue, respectively (Figures 3C and S4A–S4D).

To define the posterior identity of the developing neuromuscular system, we examined the expression of *HOX* genes by single-cell RNA sequencing and immunohistochemistry. The analysis revealed that the NMOs had maintained their initial HOX code corresponding to a posterior spinal cord identity (Figure S3B) (Dasen et al., 2005; Philippidou and Dasen, 2013). Immunofluorescence analysis for HOXC6 (brachial identity), HOXC9 (thoracic identity) and HOXC10 (posterior thoracic/lumbar identity) revealed that the NMOs have a thoracic/lumbar identity ($HOXC6^-/HOXC9^+/HOXC10^+$) (Figure S3C). $HOXC10^+$ neurons were expressing the mature neurofilament marker SMI32 (Figure S4E).

Consistent with the continuing maturation of the organoids, most spinal cord neurons were expressing the neurofilament marker SMI32 (75.6% ± 6.4%), while MNs expressing the acetylcholine (ACh)-synthesizing enzyme choline acetyltransferase (ChAT) (6.4% ± 1.4%) were found clustered in the neural part of the organoid close to the skeletal muscle (Figures S4G and S4F). Mature spinal cord neurons and MNs were reproducibly generated in similar proportions in NMOs generated by different hPSC lines and experimental batches (Figure S4G). Electron microscopy revealed the presence of longitudinally arranged, mitochondria-containing axons, the formation of synaptic clefts, and the presence of synaptic vesicles in the presynaptic neuron (Figures 3F and 3G), which suggested the formation of functional synapses. $GFAP^+$ glia cells (Figure 4A) and myelinated axons detected by the expression of myelin basic protein (MBP) (Figures 4E and 4F) were also first detected at this stage. Similar to the *in vivo* development, the number of $GFAP^+$ cells increased from day 50 (14.2% ± 4.1%) to day 150 (58.2% ± 6.8%), recapitulating the later developmental timing of glial cells *in vivo* (Figures 4A–4D).

Day 50 analyses also unveiled the maturation of the muscle part of the organoids. The formation of the basal lamina was now evident from the deposition of a continuous sheath of laminin around individual muscle fibers (Figures S5A and S5B). These muscle fibers were in contact with MN boutons expressing synaptophysin (Figure S5A). Electron microscopy revealed the development of highly organized skeletal muscle exhibiting aligned sarcomeric units with the presence of distinct Z and M lines (Figures 3D and 3E). Numerous $PAX7^+/Ki67^+$ and $PAX7^+/Ki67^-$ cells were also present in the muscle region, suggesting the presence of both proliferating muscle progenitors and satellite-like cells. The location of many $PAX7^+$ cells under the basal lamina and the detection of quiescent $PAX7^+/Ki67^-$ cells also supported the idea that satellite-like cells were present in the NMOs (Figures S5B–S5E). To further assess this, we quantified the number of $PAX7^+$ cells and the ratio of mitotically active $PAX7^+/Ki67^+$ cells in day 50, day 100, and day 150 organoids. The number of $PAX7^+/Ki67^-$ cells declined steadily from 18.53% ± 9.17% at day 50 to 8.04% ± 3.13% at day 150, consistent with continuing maturation of the muscle. The number of $PAX7^+/Ki67^+$ cells also significantly decreased from 0.93% ± 0.75% at day 50 to 0.06% ± 0.036% at day 150, suggesting that quiescent $PAX7^+$ cells persisted in day 150 month-old organoids (Figures S5E and S5F). Muscle maturation at day 150 was also documented by the presence of muscle fibers with peripheral nuclei and striations observed with Titin immunofluorescence analysis (Figure 4D). These data demonstrated muscle development and maturation in the 3D NMOs, including the generation of muscle satellite-like cells.

NMOs Develop Functional NMJs and Model Key Aspects of MG

At day 50 NMOs, we detected numerous large ACh receptor (AChR) clusters by staining for α-bungarotoxin (αBTX) contacted by $TUJ1^+$ neurites, suggesting the formation of NMJs (Figure 5A). The formation of functional NMJs in 3D was confirmed by the presence of synaptic vesicles in the presynaptic nerve terminal and by the folding of the muscle basement membrane using electron microscopy (Figure 5D). $S100\beta^+$ terminal Schwann cells capping the neuronal terminals could also be detected (Figure 5C). The generation of Schwann cells was in agreement with the presence of trunk neural crest cells in early NMOs (Figure S1G) (Frith et al., 2018). We analyzed the number of NMJs in organoids from 3 different human PSC lines and 3 different batches from each line at day 50. The results show that the number of NMJs is similar among different NMOs, batches, and hPSC lines (Figure 5B), which suggested that the formation of NMJs in 3D is independent of cell lines and experiments. Finally,

Figure 3. Self-Organization of Spinal Cord Neurons and Skeletal Muscles in NMOs

(A) Immunofluorescence analysis of NMO sections at day 50 shows the presence of neurons ($TUJ1^+$ cells) that project axons into the organized skeletal muscle region labeled with myosin skeletal fast (Fast MyHC).

(B) Schematic representation of the neuromuscular organization in the human body where spinal cord neurons from the ventral horn connect with limb skeletal muscles to form functional NMJs and control movement.

(C) Percentage of neural and muscle cells shows the reproducibility of NMO generation in at least 3 different organoids (n) from 3 different experimental batches (N) in the H9 line (n = 12, N = 3). The number of organoids analyzed (n) and the number of experiments (N) from each cell line are summarized in Table S1.

(D–G) Transmission electron microscopy reveals that day 70 organoids consist of 2 major functional compartments. NMO muscle region showing a high degree of maturation with sarcomere features such as parallel-aligned myosin-actin filaments, distinct z lines (Z) and M-bands (M), glycogen granules (Gly), and areas with grouped mitochondria (D). Higher magnification of a sarcomeric region is shown in (E). NMO neuronal region showing densely packed parallel-aligned axons and intact synapses. The neuronal axons are rich in mitochondria (Mi) and neurofilaments (F). At higher magnifications, the synapses show the formation of synaptic clefts and the presence of synaptic vesicles (SV) at the active zone (asterisks) (G).

Data are represented as mean ± SD.

See also Table S1.

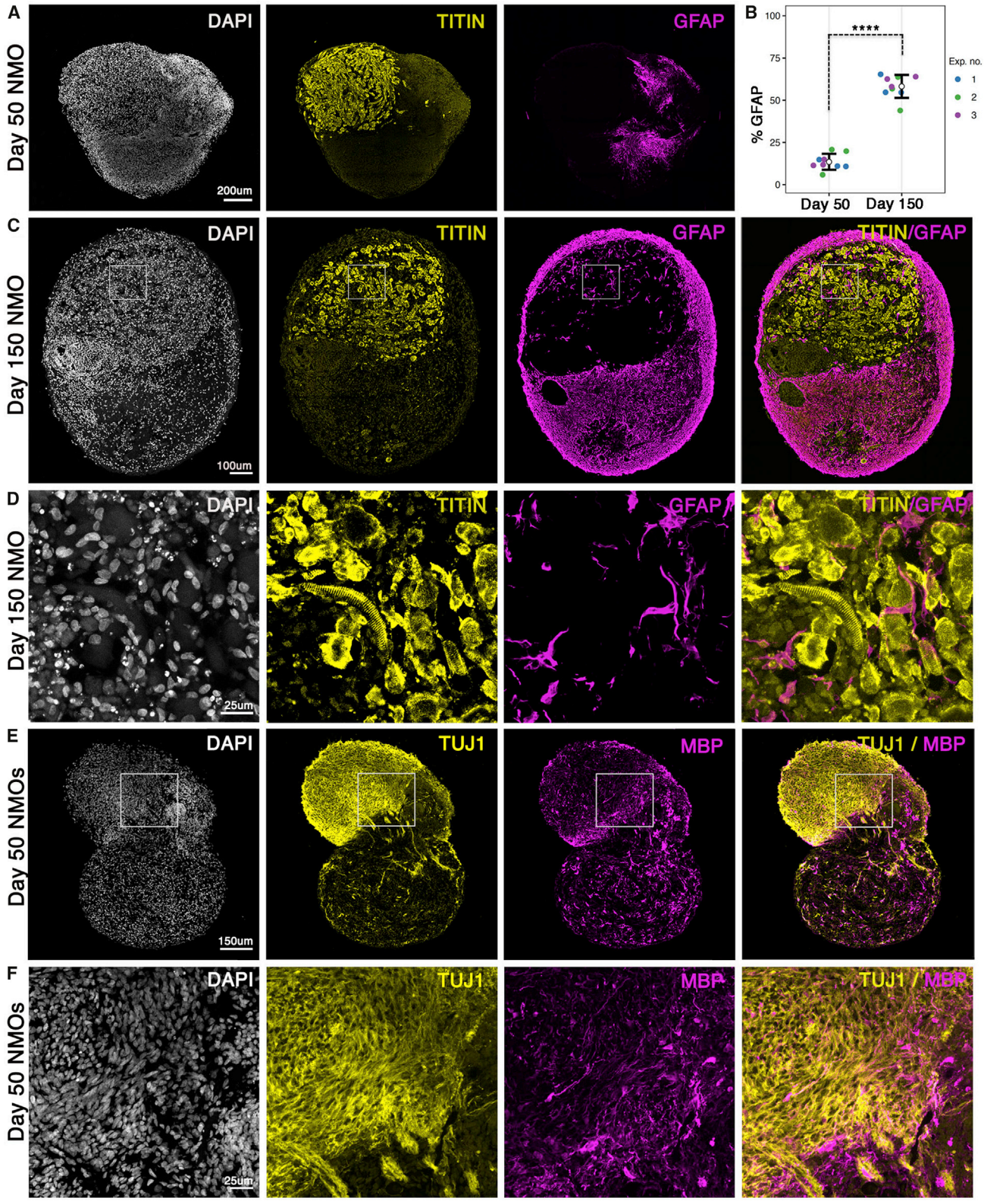

Figure 4. Glia Development and NMO Maturation between Days 50 and 150

(A) Section of whole organoid at day 50 reveals the expression of the sarcomeric protein Titin in the skeletal muscle fibers and the presence of cells that express the glial fibrillary acidic protein (GFAP).

(legend continued on next page)

and consistent with the physiological pruning process taking place during neuromuscular development (Sanes and Lichtman, 1999), the number of αBTX$^+$ clusters, normalized for the number of muscle fibers, initially declined from day 50 to day 100, whereas after that period, the number of NMJs was stable (day 150) (Figure 5B). Thus, all of the different cell types required for the formation of functional NMJs were generated and self-organized in 3D, resembling the *in vivo* process. To investigate the functionality of NMJs, we measured the contractile activity of NMOs before and after treatment with curare (10 μM), a blocker of AChRs. Treatment with curare (10 μM) blocked the contraction of the skeletal muscles, demonstrating that muscle activity was dependent upon functional NMJs (Figure 5E; Video S3).

We next sought to address whether the NMOs were suitable to model a common autoimmune disease that affects the NMJ, MG (Toyka et al., 1977). MG is caused by autoantibodies against NMJ-specific proteins such as the AChR. The autoimmune attack directed at AChRs results in the destruction of the neuromuscular endplate (Sahashi et al., 1980). To this end, we treated the NMOs with purified immunoglobulin G (IgG) fractions (300 nM total IgG) from 2 patients with MG who had high titers of autoantibodies against the AChR (see Method Details). At least 3 different organoids were incubated for 72 h with fresh human serum (2%) containing active complement and specific IgGs from each patient. The quantification of αBTX clusters in the NMOs after treatment revealed a severe reduction in the number of NMJs in the NMOs treated with patient serum compared to controls (Figures 5F and 5G). This resulted in a significant reduction in the contraction rate and amplitude in the treated NMOs (Figures 5H and 5I). These findings recapitulated key aspects of the disease pathology, suggesting that NMOs reliably model such disorders, which will be useful for future studies.

NMOs Form CPG-like Circuits

We next characterized key physiological parameters in the NMOs by calcium imaging and electrophysiological analysis using a multielectrode array (MEA) system (Figures 6 and S6). Calcium oscillations revealed spontaneous neural activity, while some neurons were showing synchronous firing at day 50 (Figure 6D; Video S2). MEA analysis detected spontaneous electrical activity from day 30 (Figure S6A). Acute glutamate treatment (50 μM) significantly increased (~12-fold) the spontaneous activity of days 30 and 50 organoids, while the specific glutamate receptor inhibitors (DL)-2-amino-5-phosphonovaleric acid (APV) (50 μM) and cyanquixaline (CNQX) (40 μM) reversibly suppressed nearly all electrical activity, demonstrating the presence of active glutamatergic neurons (Figures S6A, S6B, and S6E). In day 50 NMOs, ACh (10 μM) stimulation also resulted in a significant increase (~10-fold) in electrical activity that was rapidly and reversibly blocked by the addition of curare (10 μM) (Figures S6C and S6E). This is consistent with the observed clustering of AChR in the muscle region at this stage (Figure 5A).

To assess whether functional networks were forming between spinal cord neurons, we examined the presence of spinal cord interneurons. At day 50 NMOs, we could detect the presence of PAX2$^+$/LHX1$^+$ interneurons (characteristic of V0, V1, and dI6 identity) and CHX10$^+$ V2a excitatory pre-motor interneurons (Figures 6A–6C). To examine the organoid responses to a fictive locomotion paradigm (Marder and Bucher, 2001; Sternfeld et al., 2017), we applied a cocktail of *N*-methyl-D-aspartate (NMDA) (10 μM) and 5-hydroxytryptamine (5-HT, also known as serotonin) (40 μM), which are known to trigger the rhythmic activity of the locomotor CPGs located in the spinal cord. Such circuits are essential for coordinated MN activity (Svensson et al., 2001). Administration of these drugs instantaneously triggered strong activity that was reversibly suppressed by the administration of 1 μM tetrodotoxin (TTX), a neurotoxin that inhibits the firing of action potentials (Figure S6D). The activity became rhythmic at day 50 NMOs, suggesting the maturation of the neural networks and acquisition of CPG-like activity (Figures 6E–6G). We analyzed the activity of these neural networks by plotting the number of active electrodes and the corresponding electrical activity before and after administration of the drugs in a network grid. In this grid, node size corresponds to the number of spikes captured by each single electrode during a recording, whereas the thickness of lines connecting the nodes represents the number of times that paired firing between electrodes occurred (Figure 6G). The position of the individual NMOs in the MEA grid is shown with a dashed line. This analysis demonstrated that the stimulation of neurons at day 50 with NMDA and 5-HT resulted in a notable increase in local firings and in a dramatic increase in synchronous network activity (Figures 6F and 6G).

DISCUSSION

Neuromuscular diseases encompass a wide range of pathologies such as MN diseases (de Boer et al., 2014; Lefebvre et al., 1995), specific muscular dystrophies (Becker and Kiener, 1955; Pearce et al., 1964), and autoimmune diseases such as MG (Toyka et al., 1977). In most of these disorders, only the MNs or skeletal muscles are initially affected, leading to defects in their interaction, whereas at late stages of the disease the other cell types are also affected. Therefore, it becomes apparent that the simultaneous generation of both cell types from hPSCs in a 3D organoid model is necessary to appropriately model the mechanisms of such diseases, particularly those in which the early stages of NMJ formation are impaired.

While organoids for multiple regions of the CNS have been established (Birey et al., 2017; Jo et al., 2016; Lancaster et al.,

(B) The number of glia cells (GFAP$^+$) in NMOs significantly increased from days 50 (14.2% ± 4.1%) to 150 (58.2% ± 6.8%), consistent with the later development of glia cells *in vivo*. The number of organoids analyzed (n) and the number of experiments (N) from each cell line are summarized in Table S1. Data are represented as mean ± SD.

(C) Section of whole organoid at day 150 reveals the organized expression of the sarcomeric protein Titin in the skeletal muscle fibers and the presence of cells that express the GFAP.

(D) Higher magnification of the muscle region shows the presence of muscle striations, revealed by Titin immunofluorescence, and peripheral nucleation of the mature muscle fibers, revealed by DAPI. GFAP$^+$ glia cells are also observed in close proximity to the muscle.

(E) Myelin basic protein (MBP) is detected at day 50 in NMO, suggesting the presence of myelinated axons.

(F) Higher magnification of the neural region of the organoids, showing the presence of myelinated axons stained with MBP and TUJ1.

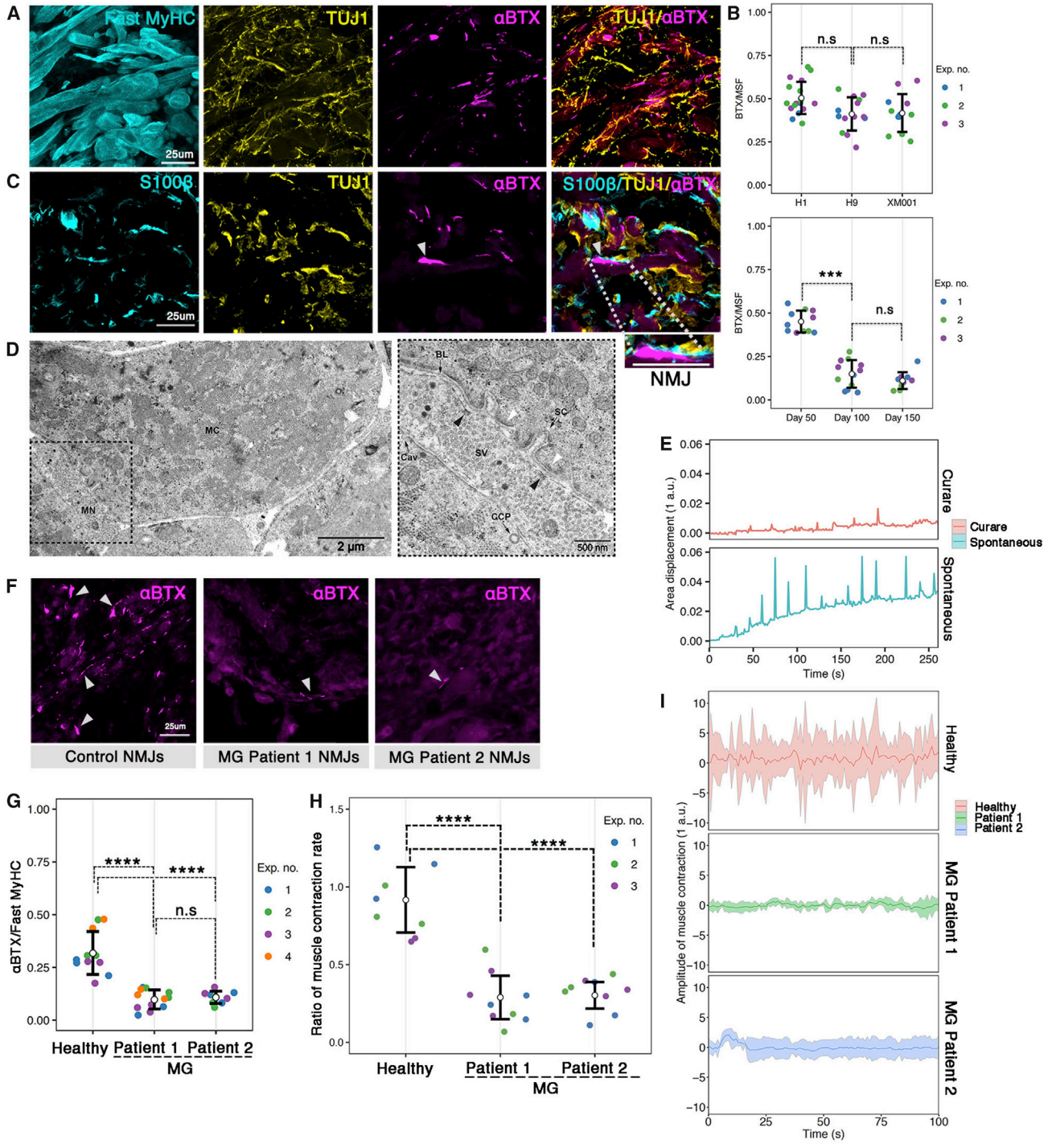

Figure 5. Formation of Functional NMJs at Day 50 NMOs Enable Modeling of MG

(A) TUJ1$^+$ neurites in contact with α-bungarotoxin$^+$ (αBTX$^+$) AChR clusters on fast-twitch skeletal muscle fibers (Fast MyHC$^+$).

(B) Quantification of the number of αBTX clusters at day 50 NMO regions normalized for the number of Fast MyHC myofibers, in at least 3 organoids from 3 different experiments in 3 different cell lines (H1, H9, and XM001), shows the reproducible generation of NMJs among different experiments and lines (n = 44, N = 9). Quantification of αBTX$^+$ clusters at regions of days 50, 100, and 150 organoids normalized for the number of Fast MyHC myofibers. The number of NMJs is significantly reduced between days 50 and 100 NMOs, whereas there is no significant difference between day 100 and 150 NMOs (n = 30, N = 9). The number of organoids analyzed (n) and the number of experiments (N) from each cell line are summarized in Table S1.

(C) Terminal Schwann cells (S100β$^+$) capping the neurites in contact with αBTX clusters characteristic of functional NMJs. The higher magnification of a relevant region is shown.

(legend continued on next page)

2013; Meinhardt et al., 2014; Ogura et al., 2018; Ranga et al., 2016; Sakaguchi et al., 2015), the generation of a complex, 3D NMO from NMPs has to our knowledge not been described before. Recently, the *in vitro* generation of NMPs from hPSCs has been instrumental in the generation of posterior spinal cord neurons and skeletal muscle cells from mouse and hPSCs in conventional monolayer cultures (Chal et al., 2015, 2016; Chal and Pourquié, 2017; Gouti et al., 2014; Lippmann et al., 2015; Maury et al., 2015). Here, we take advantage of the developmental potential of NMPs to generate a complex 3D NMO model in which 2 different tissues, spinal cord neurons and skeletal muscles, develop in parallel, self-organize, and interact to form functional neuromuscular networks. We have generated such NMOs from different hPSC lines and an iPSC line showing that the protocol works reproducibly in different experiments and cell lines.

In NMOs, spinal cord neurons, skeletal muscles, and terminal glial cells interact to generate functional NMJs that we analyzed anatomically and functionally. NMOs from all of the different hPSC lines examined started contracting in 3D between days 40 and 50 concomitant with the accumulation of αBTX clusters in the muscle fibers. Blocking AChR with curare resulted in organoid relaxation, suggesting the presence of functional NMJ between MNs and skeletal muscles in 3D. Thus, NMOs contain key, functional components of the neuromuscular system.

Complex interactions between spinal cord neurons occur during development, resulting in the generation of neuronal networks resembling CPGs. It has been previously shown that the activation of NMDA and 5-HT receptors play an important role in the initiation of locomotor rhythms in the mammalian spinal cord but also in artificial neural networks called circuitoids (Sternfeld et al., 2017). We found that stimulation with NMDA/5-HT produced rhythmic bursts of electrical activity, suggesting the establishment of network connections between interneurons and MNs in the NMOs. The generation of CPG-like networks in human NMOs will allow further studies regarding their involvement in neurodegenerative diseases. Such studies have so far been limited due to the lack of an amenable human model and have been mostly conducted in mouse models and spinal cord explant cultures.

NMOs contain key, functional components of the neuromuscular system; they are highly reproducible and can be easily maintained in culture for several months. These attributes make NMOs an attractive system to study neuromuscular disorders and to develop potential therapies. As a proof of principle, we have modeled MG, a frequent autoimmune disease that specifically disrupts NMJs and thus affects muscle contraction. NMOs treated with autoantibodies from MG patients showed severe dysfunction of the NMJs and relaxation of the muscle, recapitulating key aspects of the disease phenotype. NMOs from iPSC lines of patients with neuromuscular disorders could be used in the future to generate a completely patient-derived NMJ model in 3D. This would provide a platform to assess the effectiveness of different pharmacological agents in stabilizing the NMJ and promoting MN survival. It would also provide unprecedented access to the early stages of the diseases that precede clinical diagnosis.

The 2D or 3D co-culture approaches and 3D NMOs such as those developed here can be used in a complementary fashion as they present distinct advantages (Paşca, 2018). For example, an important advantage of the co-culture system is that it allows the generation of specific cell types from different genetic backgrounds, thus addressing the mechanism of disease only in 1 population (e.g., MNs). However, 3D cultures can be maintained for longer periods (>1 year) and provide access to diverse cell types at different maturation states. Thus, NMOs are better suited to study the contribution of each cell type, including terminal Schwann cells, at different stages of NMJ development and maturation that may contribute to the disease phenotype.

An important caveat of 2D co-culture systems has been the lack of functional mature skeletal muscle fibers generated from hPSCs. Most studies relied on the use of primary skeletal muscle from human biopsies or immature muscles generated separately from hPSCs. These approaches lack the timely interaction between MNs and muscle fibers that are necessary for NMJ maturation. In addition, it has been recently shown that the maturation of skeletal muscles in 3D is more advanced than the one achieved in 2D culture conditions (Afshar Bakooshli et al., 2019). Crucially, input from the MNs is required for the proper muscle maturation and generation of functional NMJs (Machado et al., 2019; Misgeld et al., 2002; Steinbeck et al., 2016). Therefore, in co-culture studies, the chemical or optogenetic stimulation of MNs has been used to activate the clustering of AChRs and to induce the formation of functional NMJs (Afshar Bakooshli et al., 2019; Machado et al., 2019; Steinbeck et al., 2016). This adds a degree of complexity and variability to such systems. It is important to note here that in the 3D NMO system, the clustering of AChR and the formation of functional NMJs happens in the absence of exogenous stimuli and in minimal culture conditions because MNs, skeletal muscles, and Schwann cells co-develop and interact in the system from its inception. In addition, NMOs support the contractility of maturing myofibers. Such contractility

(D) Transmission electron microscopy reveals that many axons are positioned close to muscle cells and some form NMJs. The muscle cell (MC) displays characteristic features such as a basal lamina (BL), protein-rich densities, and invaginations of the plasma membrane at the motor neuron-muscle contact site (synaptic cleft [SC]). The neighboring MN axon shows pre-synaptic densities and synaptic vesicles close to the MC. Black and white arrowheads indicate pre- and post-synaptic densities, respectively.

(E) Graphs showing displacement of a region of interest (ROI) in 250-s recordings of spontaneous contractions before and after administration of 10 μM curare.

(F) Representative images of αBTX clusters in control and MG patient-treated NMOs after 3 days of treatment with patient IgGs.

(G) Quantification of αBTX clusters in control NMOs at day 50 and NMOs treated with autoantibodies from MG patients 1 and 2, respectively, shows a significant reduction in the number of αBTX clusters in MG NMOs. The number of organoids analyzed (n) and the number of experiments (N) from each cell line are summarized in Table S1.

(H and I) The ratio of muscle contraction rate (H) and the amplitude of muscle contraction (I) are significantly reduced following a 3-day treatment with MG IgG autoantibodies, but they are not affected by treatment with IgG from a healthy subject. The number of organoids analyzed (n) and the number of experiments (N) from each cell line are summarized in Table S1.

Data are represented as mean ± SD.

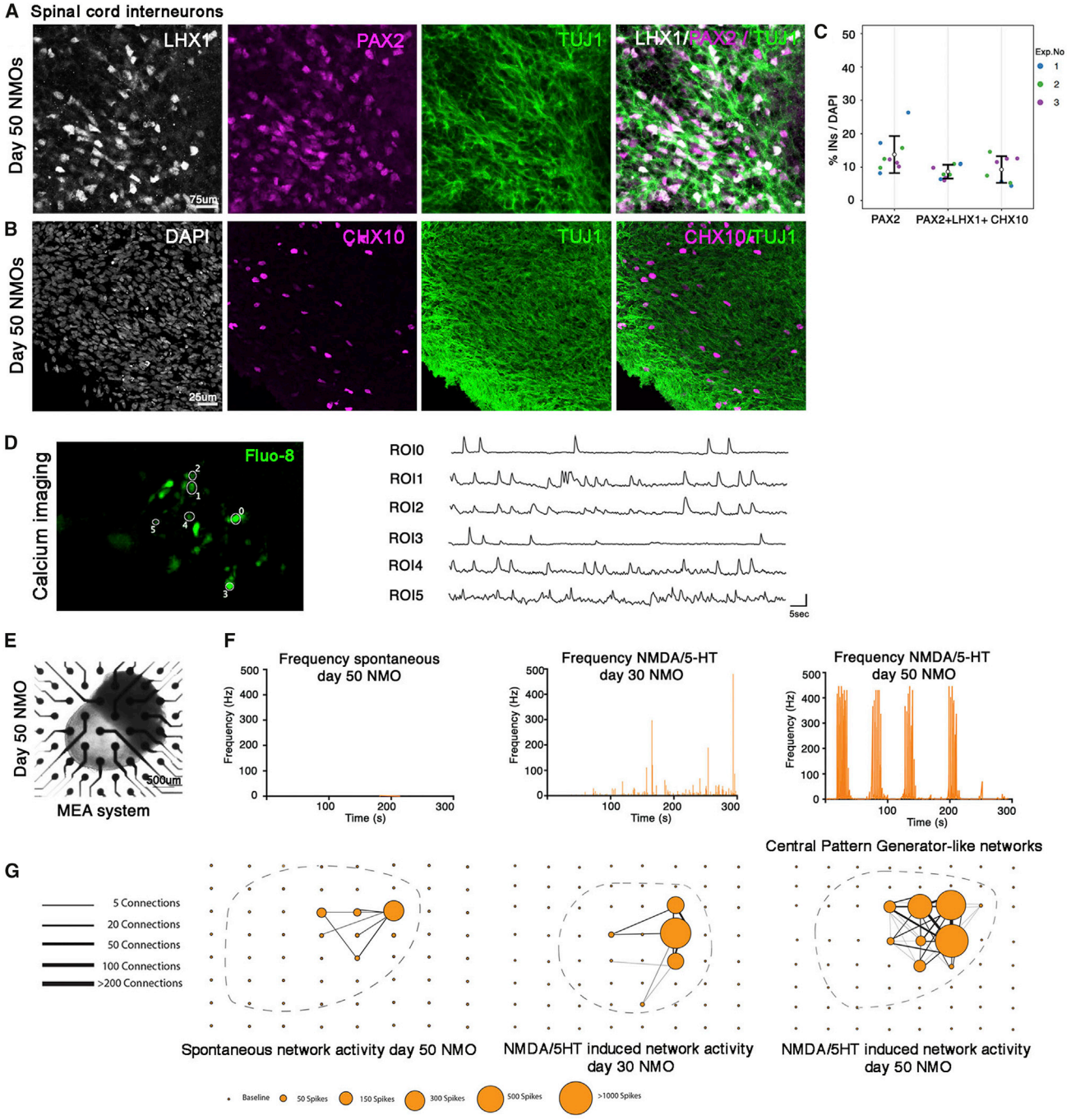

Figure 6. Formation of Functional Spinal Cord Networks with CPG-like Activity in NMOs

(A and B) Immunofluorescence analysis of PAX2/LHX1 expressed in spinal cord (V0, V1, and dI6) interneurons (A) and CHX10 expressed in V2a premotor interneurons (B) reveals their presence in the neural part of day 50 NMOs.

(C) Quantification of $PAX2^+$ (13.8% ± 5.5%), $PAX2^+/LHX1^+$ (8.6% ± 2%), and $CHX10^+$ (9.3% ± 4%) interneurons in NMOs at day 50 (n = 9, N = 3). The number of organoids analyzed (n) and the number of experiments (N) from each cell line are summarized in Table S1.

(D) Calcium imaging at day 50 reveals the spontaneous activity of the NMOs (n = 5). See also Video S2.

(E) Bright-field imaging of day 50 NMO in the MEA system.

(F) Plot showing the average spike frequency before (spontaneous [sns]) and after the application of 50 μM NMDA and 40 μM 5-HT in days 30 and 50 NMOs. Day 50 NMOs show CPG-like activity.

(G) Network graph showing the connectivity between electrodes recording spontaneous (left) or 50 μM NMDA/40 μM 5-HT at day 30 (middle) or 50 μM NMDA/40 μM 5-HT at day 50 stimulated electrical activity. Line thickness represents the number of times the paired firing occurred between electrodes, while node size shows the number of spikes captured by each single electrode during a recording. The stimulation of neurons at day 50 with NMDA/5-HT showed increased single firings and an increase in paired electrode spikes. The position of the individual NMOs in the MEA grid is shown with a dashed line.

does not usually develop in 2D co-culture systems, possibly due to the disadvantages of the cell culture substrates, which necessitates further studies modifying the 2D microenvironment. Similarly, in the future it will be important to identify the correct time window during which skeletal muscles need to receive input from the MN to develop intrinsically functional NMJ networks that do not rely on exogenous stimuli. Conditions that allow the simultaneous generation of MNs, skeletal muscle fibers, and terminal Schwann cells in 2D may be useful for this purpose.

Further refinement of the anterior-posterior identity of NMOs to generate all of the different segments of the spinal cord and associated musculature could provide novel insights into the selective vulnerability of specific types of MNs to disease. An additional future challenge will be to achieve full maturation of the NMOs by providing input from the motor cortex. The ability of cerebral organoids to form extracortical projecting tracts, which innervate and activate mouse spinal cord-muscle explants has been described recently (Giandomenico et al., 2019). Thus, the establishment of NMOs affords the opportunity to establish and study the formation of these complex networks in an all-human *in vitro* 3D model.

One of the most exciting opportunities for the future is to use this NMO system to understand how the trunk neuromuscular system is formed in humans and how the functional neuromuscular networks emerge during development. This would also allow the exploration of the possible developmental origins of neuromuscular diseases.

STAR★METHODS

Detailed methods are provided in the online version of this paper and include the following:

- KEY RESOURCES TABLE
- LEAD CONTACT AND MATERIALS AVAILABILITY
- EXPERIMENTAL MODEL AND SUBJECT DETAILS
  - Human pluripotent stem cell lines and culture conditions
  - Human samples
- METHOD DETAILS
  - *In vitro* generation of NMPs from human pluripotent stem cells
  - Generation of neuromuscular organoids in 3D
  - Immunohistochemical analysis of organoids
  - Reverse transcription – Quantitative PCR Analysis
  - Live imaging of organoids
  - Electron microscopy of organoids
  - Organoids cell dissociation for scRNaseq analysis
  - Tag incubation for single-cell RNA-sequencing analysis
  - Single-cell RNA-sequencing
  - Mapping and extraction of single-cell mRNA transcript counts
  - Single-cell data analysis
  - Calcium Imaging of organoids
  - Contraction analysis
  - Cell counting and statistical analysis
  - Microelectrode array (MEA) recording and analysis
  - Myasthenia gravis disease modeling
- QUANTIFICATION AND STATISTICAL ANALYSIS
- DATA AND CODE AVAILABILITY

SUPPLEMENTAL INFORMATION

Supplemental Information can be found online at https://doi.org/10.1016/j.stem.2019.12.007.

ACKNOWLEDGMENTS

We thank Heiko Lickert and Ralf Kühn, who kindly provided us with the XM001 iPSC line. We thank Sebastian Diecke, head of the Max Delbrück Center (MDC) pluripotent stem cell facility, and Bettina Purfürst, head of the electron microscopy facility, for support. We thank Caroline Braeuning, Nicole Greiger, and Sandra Schlosser for excellent technical assistance. We thank Marie-Sophie Bittner for performing the human stem cell differentiation experiments in 2D. We are grateful to Anthony Gavalas, James Briscoe, and Niccolò Zampieri for critical reading of the manuscript. This work was supported by the Max Delbrück Center (MDC), which receives its core funding from the Helmholtz Association of German Research Centers, and a European Research Council (ERC) recognition award grant to M.G. from the Helmholtz Association of German Research Centers (ERC-RA-0030).

AUTHOR CONTRIBUTIONS

M.G. conceived the project and experimental design, performed and analyzed the experiments, and wrote the manuscript. J.M.F.M designed and performed the experiments and performed the data analysis. C.F. and R.V. analyzed the single-cell data under the supervision of S. Sauer. A.U. performed the 2D hPSC differentiation experiments. S.K. performed the electron microscopy analysis of the NMOs. L.K. and I.H. performed the immunofluorescence analysis experiments and provided technical support. P.L.R helped with the analysis of the calcium and muscle contraction experiments. E.G. and S. Spuler. provided the MG patient samples. C.B., J.M.F.M., P.L.R., C.F., S. Sauer. and S. Spuler. revised the manuscript.

DECLARATION OF INTERESTS

The authors declare no competing interests.

Received: March 18, 2019
Revised: September 30, 2019
Accepted: December 16, 2019
Published: January 16, 2020

REFERENCES

Adler, D., and Kelly, S.T. (2019). vioplot: violin plot. R package version 0.3.4, https://github.com/TomKellyGenetics/vioplot.

Afshar Bakooshli, M., Lippmann, E.S., Mulcahy, B., Iyer, N., Nguyen, C.T., Tung, K., Stewart, B.A., van den Dorpel, H., Fuehrmann, T., Shoichet, M., et al. (2019). A 3D culture model of innervated human skeletal muscle enables studies of the adult neuromuscular junction. eLife *8*, e44530.

Becht, E., McInnes, L., Healy, J., Dutertre, C.A., Kwok, I.W.H., Ng, L.G., Ginhoux, F., and Newell, E.W. (2018). Dimensionality reduction for visualizing single-cell data using UMAP. Nat. Biotechnol. *37*, 38–44.

Becker, P.E., and Kiener, F. (1955). [A new x-chromosomal muscular dystrophy]. Arch. Psychiatr. Nervenkr. Z. Gesamte Neurol. Psychiatr. *193*, 427–448.

Birey, F., Andersen, J., Makinson, C.D., Islam, S., Wei, W., Huber, N., Fan, H.C., Metzler, K.R.C., Panagiotakos, G., Thom, N., et al. (2017). Assembly of functionally integrated human forebrain spheroids. Nature *545*, 54–59.

Brassard, J.A., and Lutolf, M.P. (2019). Engineering Stem Cell Self-organization to Build Better Organoids. Cell Stem Cell *24*, 860–876.

Broutier, L., Andersson-Rolf, A., Hindley, C.J., Boj, S.F., Clevers, H., Koo, B.K., and Huch, M. (2016). Culture and establishment of self-renewing human and mouse adult liver and pancreas 3D organoids and their genetic manipulation. Nat. Protoc. *11*, 1724–1743.

Cambray, N., and Wilson, V. (2002). Axial progenitors with extensive potency are localised to the mouse chordoneural hinge. Development *129*, 4855–4866.

Chal, J., and Pourquié, O. (2017). Making muscle: skeletal myogenesis *in vivo* and *in vitro*. Development *144*, 2104–2122.

Chal, J., Oginuma, M., Al Tanoury, Z., Gobert, B., Sumara, O., Hick, A., Bousson, F., Zidouni, Y., Mursch, C., Moncuquet, P., et al. (2015). Differentiation of pluripotent stem cells to muscle fiber to model Duchenne muscular dystrophy. Nat. Biotechnol. *33*, 962–969.

Chal, J., Al Tanoury, Z., Hestin, M., Gobert, B., Aivio, S., Hick, A., Cherrier, T., Nesmith, A.P., Parker, K.K., and Pourquié, O. (2016). Generation of human muscle fibers and satellite-like cells from human pluripotent stem cells in vitro. Nat. Protoc. *11*, 1833–1850.

Darabid, H., Perez-Gonzalez, A.P., and Robitaille, R. (2014). Neuromuscular synaptogenesis: coordinating partners with multiple functions. Nat. Rev. Neurosci. *15*, 703–718.

Dasen, J.S., Tice, B.C., Brenner-Morton, S., and Jessell, T.M. (2005). A Hox regulatory network establishes motor neuron pool identity and target-muscle connectivity. Cell *123*, 477–491.

de Boer, A.S., Koszka, K., Kiskinis, E., Suzuki, N., Davis-Dusenbery, B.N., and Eggan, K. (2014). Genetic validation of a therapeutic target in a mouse model of ALS. Sci. Transl. Med. *6*, 248ra104.

Deschamps, J., and Duboule, D. (2017). Embryonic timing, axial stem cells, chromatin dynamics, and the Hox clock. Genes Dev. *31*, 1406–1416.

Edgar, R., Domrachev, M., and Lash, A.E. (2002). Gene Expression Omnibus: NCBI gene expression and hybridization array data repository. Nucleic Acids Res. *30*, 207–210.

Eiraku, M., and Sasai, Y. (2012). Self-formation of layered neural structures in three-dimensional culture of ES cells. Curr. Opin. Neurobiol. *22*, 768–777.

Engel, A.G. (2018). Congenital Myasthenic Syndromes in 2018. Curr. Neurol. Neurosci. Rep. *18*, 46.

Forlani, S., Lawson, K.A., and Deschamps, J. (2003). Acquisition of Hox codes during gastrulation and axial elongation in the mouse embryo. Development *130*, 3807–3819.

Frith, T.J., Granata, I., Wind, M., Stout, E., Thompson, O., Neumann, K., Stavish, D., Heath, P.R., Ortmann, D., Hackland, J.O., et al. (2018). Human axial progenitors generate trunk neural crest cells in vitro. eLife *7*, e35786.

Giandomenico, S.L., Mierau, S.B., Gibbons, G.M., Wenger, L.M.D., Masullo, L., Sit, T., Sutcliffe, M., Boulanger, J., Tripodi, M., Derivery, E., et al. (2019). Cerebral organoids at the air-liquid interface generate diverse nerve tracts with functional output. Nat. Neurosci. *22*, 669–679.

Gouti, M., Tsakiridis, A., Wymeersch, F.J., Huang, Y., Kleinjung, J., Wilson, V., and Briscoe, J. (2014). In vitro generation of neuromesodermal progenitors reveals distinct roles for wnt signalling in the specification of spinal cord and paraxial mesoderm identity. PLoS Biol. *12*, e1001937.

Gouti, M., Delile, J., Stamataki, D., Wymeersch, F.J., Huang, Y., Kleinjung, J., Wilson, V., and Briscoe, J. (2017). A Gene Regulatory Network Balances Neural and Mesoderm Specification during Vertebrate Trunk Development. Dev. Cell *41*, 243–261.e7.

Hayes, J.A., Papagiakoumou, E., Ruffault, P.-L., Emiliani, V., and Fortin, G. (2018). Computer-aided neurophysiology and imaging with open-source PhysImage. Journal of Neurophysiology *120*, 23–36.

Henrique, D., Abranches, E., Verrier, L., and Storey, K.G. (2015). Neuromesodermal progenitors and the making of the spinal cord. Development *142*, 2864–2875.

Huch, M., Gehart, H., van Boxtel, R., Hamer, K., Blokzijl, F., Verstegen, M.M., Ellis, E., van Wenum, M., Fuchs, S.A., de Ligt, J., et al. (2015). Long-term culture of genome-stable bipotent stem cells from adult human liver. Cell *160*, 299–312.

Jo, J., Xiao, Y., Sun, A.X., Cukuroglu, E., Tran, H.D., Göke, J., Tan, Z.Y., Saw, T.Y., Tan, C.P., Lokman, H., et al. (2016). Midbrain-like Organoids from Human Pluripotent Stem Cells Contain Functional Dopaminergic and Neuromelanin-Producing Neurons. Cell Stem Cell *19*, 248–257.

Kimelman, D. (2016). Tales of Tails (and Trunks): Forming the Posterior Body in Vertebrate Embryos. Curr. Top. Dev. Biol. *116*, 517–536.

La Manno, G., Soldatov, R., Zeisel, A., Braun, E., Hochgerner, H., Petukhov, V., Lidschreiber, K., Kastriti, M.E., Lönnerberg, P., Furlan, A., et al. (2018). RNA velocity of single cells. Nature *560*, 494–498.

Lancaster, M.A., Renner, M., Martin, C.A., Wenzel, D., Bicknell, L.S., Hurles, M.E., Homfray, T., Penninger, J.M., Jackson, A.P., and Knoblich, J.A. (2013). Cerebral organoids model human brain development and microcephaly. Nature *501*, 373–379.

Lefebvre, S., Bürglen, L., Reboullet, S., Clermont, O., Burlet, P., Viollet, L., Benichou, B., Cruaud, C., Millasseau, P., Zeviani, M., et al. (1995). Identification and characterization of a spinal muscular atrophy-determining gene. Cell *80*, 155–165.

Lippmann, E.S., Williams, C.E., Ruhl, D.A., Estevez-Silva, M.C., Chapman, E.R., Coon, J.J., and Ashton, R.S. (2015). Deterministic HOX patterning in human pluripotent stem cell-derived neuroectoderm. Stem Cell Reports *4*, 632–644.

Machado, C.B., Pluchon, P., Harley, P., Rigby, M., Gonzalez Sabater, V., Stevenson, D.C., Hynes, S., Lowe, A., Burrone, J., Viasnoff, V., et al. (2019). In Vitro Modelling of Nerve-Muscle Connectivity in a Compartmentalised Tissue Culture Device. Adv. Biosyst. *3*, 1800307.

Maffioletti, S.M., Sarcar, S., Henderson, A.B.H., Mannhardt, I., Pinton, L., Moyle, L.A., Steele-Stallard, H., Cappellari, O., Wells, K.E., Ferrari, G., et al. (2018). Three-Dimensional Human iPSC-Derived Artificial Skeletal Muscles Model Muscular Dystrophies and Enable Multilineage Tissue Engineering. Cell Rep. *23*, 899–908.

Marder, E., and Bucher, D. (2001). Central pattern generators and the control of rhythmic movements. Curr. Biol. *11*, R986–R996.

Maury, Y., Côme, J., Piskorowski, R.A., Salah-Mohellibi, N., Chevaleyre, V., Peschanski, M., Martinat, C., and Nedelec, S. (2015). Combinatorial analysis of developmental cues efficiently converts human pluripotent stem cells into multiple neuronal subtypes. Nat. Biotechnol. *33*, 89–96.

Meinhardt, A., Eberle, D., Tazaki, A., Ranga, A., Niesche, M., Wilsch-Bräuninger, M., Stec, A., Schackert, G., Lutolf, M., and Tanaka, E.M. (2014). 3D reconstitution of the patterned neural tube from embryonic stem cells. Stem Cell Reports *3*, 987–999.

Metzis, V., Steinhauser, S., Pakanavicius, E., Gouti, M., Stamataki, D., Ivanovitch, K., Watson, T., Rayon, T., Mousavy Gharavy, S.N., Lovell-Badge, R., et al. (2018). Nervous System Regionalization Entails Axial Allocation before Neural Differentiation. Cell *175*, 1105–1118.e7.

Miller, T.M., Kim, S.H., Yamanaka, K., Hester, M., Umapathi, P., Arnson, H., Rizo, L., Mendell, J.R., Gage, F.H., Cleveland, D.W., and Kaspar, B.K. (2006). Gene transfer demonstrates that muscle is not a primary target for non-cell-autonomous toxicity in familial amyotrophic lateral sclerosis. Proc. Natl. Acad. Sci. USA *103*, 19546–19551.

Misgeld, T., Burgess, R.W., Lewis, R.M., Cunningham, J.M., Lichtman, J.W., and Sanes, J.R. (2002). Roles of neurotransmitter in synapse formation: development of neuromuscular junctions lacking choline acetyltransferase. Neuron *36*, 635–648.

Morizane, R., Lam, A.Q., Freedman, B.S., Kishi, S., Valerius, M.T., and Bonventre, J.V. (2015). Nephron organoids derived from human pluripotent stem cells model kidney development and injury. Nat. Biotechnol. *33*, 1193–1200.

Nicolau, S., Kao, J.C., and Liewluck, T. (2019). Trouble at the junction: When myopathy and myasthenia overlap. Muscle Nerve *60*, 648–657.

Ogura, T., Sakaguchi, H., Miyamoto, S., and Takahashi, J. (2018). Three-dimensional induction of dorsal, intermediate and ventral spinal cord tissues from human pluripotent stem cells. Development *145*, dev162214.

Olivera-Martinez, I., Harada, H., Halley, P.A., and Storey, K.G. (2012). Loss of FGF-dependent mesoderm identity and rise of endogenous retinoid signalling determine cessation of body axis elongation. PLoS Biol. *10*, e1001415.

Osafune, K., Caron, L., Borowiak, M., Martinez, R.J., Fitz-Gerald, C.S., Sato, Y., Cowan, C.A., Chien, K.R., and Melton, D.A. (2008). Marked differences in differentiation propensity among human embryonic stem cell lines. Nat. Biotechnol. *26*, 313–315.

Osaki, T., Uzel, S.G.M., and Kamm, R.D. (2018). Microphysiological 3D model of amyotrophic lateral sclerosis (ALS) from human iPS-derived muscle cells and optogenetic motor neurons. Sci. Adv. *4*, eaat5847.

Paşca, S.P. (2018). The rise of three-dimensional human brain cultures. Nature *553*, 437–445.

Paşca, A.M., Sloan, S.A., Clarke, L.E., Tian, Y., Makinson, C.D., Huber, N., Kim, C.H., Park, J.Y., O'Rourke, N.A., Nguyen, K.D., et al. (2015). Functional cortical neurons and astrocytes from human pluripotent stem cells in 3D culture. Nat. Methods *12*, 671–678.

Pearce, J.M., Pennington, R.J., and Walton, J.N. (1964). Serum Enzyme Studies in Muscle Disease. III. Serum Creatine Kinase Activity in Relatives of Patients with the Duchenne Type of Muscular Dystrophy. J. Neurol. Neurosurg. Psychiatry *27*, 181–185.

Philippidou, P., and Dasen, J.S. (2013). Hox genes: choreographers in neural development, architects of circuit organization. Neuron *80*, 12–34.

Ranga, A., Girgin, M., Meinhardt, A., Eberle, D., Caiazzo, M., Tanaka, E.M., and Lutolf, M.P. (2016). Neural tube morphogenesis in synthetic 3D microenvironments. Proc. Natl. Acad. Sci. USA *113*, E6831–E6839.

Rowe, R.G., and Daley, G.Q. (2019). Induced pluripotent stem cells in disease modelling and drug discovery. Nat. Rev. Genet. *20*, 377–388.

Sahashi, K., Engel, A.G., Lambert, E.H., and Howard, F.M., Jr. (1980). Ultrastructural localization of the terminal and lytic ninth complement component (C9) at the motor end-plate in myasthenia gravis. J. Neuropathol. Exp. Neurol. *39*, 160–172.

Sakaguchi, H., Kadoshima, T., Soen, M., Narii, N., Ishida, Y., Ohgushi, M., Takahashi, J., Eiraku, M., and Sasai, Y. (2015). Generation of functional hippocampal neurons from self-organizing human embryonic stem cell-derived dorsomedial telencephalic tissue. Nat. Commun. *6*, 8896.

Sances, S., Bruijn, L.I., Chandran, S., Eggan, K., Ho, R., Klim, J.R., Livesey, M.R., Lowry, E., Macklis, J.D., Rushton, D., et al. (2016). Modeling ALS with motor neurons derived from human induced pluripotent stem cells. Nat. Neurosci. *19*, 542–553.

Sanes, J.R., and Lichtman, J.W. (1999). Development of the vertebrate neuromuscular junction. Annu. Rev. Neurosci. *22*, 389–442.

Santhanam, N., Kumanchik, L., Guo, X., Sommerhage, F., Cai, Y., Jackson, M., Martin, C., Saad, G., McAleer, C.W., Wang, Y., et al. (2018). Stem cell derived phenotypic human neuromuscular junction model for dose response evaluation of therapeutics. Biomaterials *166*, 64–78.

Schindelin, J., Arganda-Carreras, I., Frise, E., Kaynig, V., Longair, M., Pietzsch, T., Preibisch, S., Rueden, C., Saalfeld, S., Schmid, B., et al. (2012). Fiji: an open-source platform for biological-image analysis. Nat. Methods *9*, 676–682.

Spence, J.R., Mayhew, C.N., Rankin, S.A., Kuhar, M.F., Vallance, J.E., Tolle, K., Hoskins, E.E., Kalinichenko, V.V., Wells, S.I., Zorn, A.M., et al. (2011). Directed differentiation of human pluripotent stem cells into intestinal tissue in vitro. Nature *470*, 105–109.

Steinbeck, J.A., Jaiswal, M.K., Calder, E.L., Kishinevsky, S., Weishaupt, A., Toyka, K.V., Goldstein, P.A., and Studer, L. (2016). Functional Connectivity under Optogenetic Control Allows Modeling of Human Neuromuscular Disease. Cell Stem Cell *18*, 134–143.

Sternfeld, M.J., Hinckley, C.A., Moore, N.J., Pankratz, M.T., Hilde, K.L., Driscoll, S.P., Hayashi, M., Amin, N.D., Bonanomi, D., Gifford, W.D., et al. (2017). Speed and segmentation control mechanisms characterized in rhythmically-active circuits created from spinal neurons produced from genetically-tagged embryonic stem cells. eLife *6*, e21540.

Stoeckius, M., Zheng, S., Houck-Loomis, B., Hao, S., Yeung, B.Z., Mauck, W.M., 3rd, Smibert, P., and Satija, R. (2018). Cell Hashing with barcoded antibodies enables multiplexing and doublet detection for single cell genomics. Genome Biol. *19*, 224.

Stuart, T., Butler, A., Hoffman, P., Hafemeister, C., Papalexi, E., Mauck, W.M., 3rd, Hao, Y., Stoeckius, M., Smibert, P., and Satija, R. (2019). Comprehensive Integration of Single-Cell Data. Cell *177*, 1888–1902.e21.

Subramanian, A., Tamayo, P., Mootha, V.K., Mukherjee, S., Ebert, B.L., Gillette, M.A., Paulovich, A., Pomeroy, S.L., Golub, T.R., Lander, E.S., and Mesirov, J.P. (2005). Gene set enrichment analysis: a knowledge-based approach for interpreting genome-wide expression profiles. Proc. Natl. Acad. Sci. USA *102*, 15545–15550.

Svensson, E., Grillner, S., and Parker, D. (2001). Gating and braking of short- and long-term modulatory effects by interactions between colocalized neuromodulators. J. Neurosci. *21*, 5984–5992.

Tirosh, I., Venteicher, A.S., Hebert, C., Escalante, L.E., Patel, A.P., Yizhak, K., Fisher, J.M., Rodman, C., Mount, C., Filbin, M.G., et al. (2016). Single-cell RNA-seq supports a developmental hierarchy in human oligodendroglioma. Nature *539*, 309–313.

Toyka, K.V., Drachman, D.B., Griffin, D.E., Pestronk, A., Winkelstein, J.A., Fishbeck, K.H., and Kao, I. (1977). Myasthenia gravis. Study of humoral immune mechanisms by passive transfer to mice. N. Engl. J. Med. *296*, 125–131.

Tzouanacou, E., Wegener, A., Wymeersch, F.J., Wilson, V., and Nicolas, J.F. (2009). Redefining the progression of lineage segregations during mammalian embryogenesis by clonal analysis. Dev. Cell *17*, 365–376.

Verrier, L., Davidson, L., Gierliński, M., Dady, A., and Storey, K.G. (2018). Neural differentiation, selection and transcriptomic profiling of human neuromesodermal progenitor-like cells *in vitro*. Development *145*, dev166215.

Wang, X., Sterr, M., Burtscher, I., Chen, S., Hieronimus, A., Machicao, F., Staiger, H., Häring, H.U., Lederer, G., Meitinger, T., et al. (2018). Genome-wide analysis of PDX1 target genes in human pancreatic progenitors. Mol. Metab. *9*, 57–68.

Wickham, H. (2016). ggplot2: Elegant Graphics for Data Analysis (Springer-Verlag New York).

Wilson, V., Olivera-Martinez, I., and Storey, K.G. (2009). Stem cells, signals and vertebrate body axis extension. Development *136*, 1591–1604.

STAR★METHODS

KEY RESOURCES TABLE

REAGENT or RESOURCE	SOURCE	IDENTIFIER
Antibodies		
Goat anti-ChAT	Millipore	Cat.No.: AB144P; RRID: AB_2079751
Goat anti-Sox1	R&D	Cat.No.: AF3369; RRID: AB_2239879
Goat anti-T/Bra	R&D	Cat.No.: AF2085; RRID: AB_2200235
Goat anti-Synaptophysin	R&D	Cat.No.: AF5555; RRID: AB_2198864
Rabbit anti-Sox2	Millipore	Cat.No.: AB5603; RRID: AB_2286686
Rabbit anti-Cadherin 6	Cell Signaling	Cat.No.: 48111S;RRID: AB_2799334
Rabbit anti-HoxC10	Abcam	Cat.No.: AB153904; RRID: AB_2687827
Rabbit anti-β tubulin III/Tuj1	Biozol	Cat.No.: GTX129913-25
Rabbit anti-Laminin	Abcam	Cat.No.: AB11575; RRID: AB_298179
Rabbit anti S100-β	Abcam	Cat.No.: AB52642; RRID: AB_882426
Rabbit anti-Ki67	Abcam	Cat.No.: AB15580; RRID: AB_443209
Rabbit anti-GFAP	Sigma Aldrich	Cat.No.: SAB5600060
Rabbit anti-Desmin	Abcam	Cat.No.: AB15200; RRID: AB_301744
Rabbit anti-Olig2	Millipore	Cat.No.: AB9610; RRID: AB_570666
Mouse anti-Pax3	DSHB	Cat.No.: Pax3; RRID: AB_528426
Mouse anti-HoxC9	Abcam	Cat.No.: AB50839; RRID: AB_880494
Mouse anti-Fast Myosin Heavy Chain	Sigma Aldrich	Cat.No.: M1570; RRID: AB_2147168
Mouse anti-Pax7	DSHB	Cat.No.: PAX7 s; RRID: AB_528428
Mouse anti-SMI32	Biolegend	Cat.No.: 801701; RRID: AB_2564642
Mouse anti-Titin	DSHB	Cat.No.: 9D10; RRID: AB_528491
Mouse anti-Islet1&2	DSHB	Cat.No.:39.4D5; RRID: AB_2314683
Mouse anti-MyoD1	BD	Cat.No.: 554130; RRID: AB_395255
Alexa 647 Conjugate α-bungarotoxin	Thermo Fisher	Cat.No.: B35450
Mouse anti-Lhx1,2	DSHB	Cat.No.: 4F2
Sheep anti-Chx10	Abcam	Cat.No.: AB16141; RRID: AB_302278
Rabbit anti-Pax2	Biozol	Cat.No.: BLD-901001
Rat anti-Myelin Basic Protein	Millipore	Cat.No.: MAB386; RRID: RRID:AB_94975
Rabbit anti-Sox10	Abcam	Cat.No.: AB155279; RRID: AB_2650603
Rabbit anti-Sox9	Cell Signaling	Cat.No.: 82630; RRID:AB_2665492
Chemicals		
mTESR1	Stem Cell Technologies	85875
DMEM F-12	Life Technologies	11320033
Neurobasal Medium	Life Technologies	21103049
MEM Non-Essential Amino Acids	Life Technologies	11140050
Penicillin-Streptomycin	Life Technologies	15140122
GlutaMAX	Life Technologies	35050061
β-Mercaptoethanol	Life Technologies	31350010
N2	Life Technologies	17502001
B27	Life Technologies	17504044
Geltrex	Life Technologies	A1413301
Matrigel	Corning	354277
Versene	Life Technologies	15040066
Accutase	Life Technologies	A1110501
Bovine Serum Albumin	Sigma Aldrich	A9418

(*Continued on next page*)

Continued

REAGENT or RESOURCE	SOURCE	IDENTIFIER
Gelatin	Sigma Aldrich	G1890
Sucrose	Sigma Aldrich	84097
Y-27632	Tocris Bioscience	1254/10
bFGF	R&D	233-FB
CHIR99021	Tocris Bioscience	4423/50
IGF	Peprotech	100-11
HGF	Peprotech	315-23
Glutamate	Genaxxon Bioscience	M6102
Acetylcholine	Sigma Aldrich	A6625
NMDA	Sigma Aldrich	M3262
5-HT	Sigma Aldrich	H9523
APV	Sigma Aldrich	A5282
CNQX	Sigma Aldrich	C127
Curare	Sigma Aldrich	T2379
TTX	Alomone Labs	T-550
Fluo-8	Abcam	AB142773
DAPI	Life Technologies	D1306
Immunoselect Antifading Mounting Medium	Dianova	SCR-038447
Human IgG	Sigma Aldrich	I4506
Commercial Assays		
RNA Extraction RNeasy Kit	QIAGEN	74104
RNase-Free DNase Set	QIAGEN	79254
Chromium™ Single Cell 3′ Library & Gel Bead Kit v2	10X Genomics	120237
Chromium™ Single Cell 3′ Library & Gel Bead Kit v3	10X Genomics	1000092
DNA HS Kit	Agilent	DNF-488-0500
KAPA Library Quantification Kit	Roche	KK4824
Chromium™ Single Cell Chip A Kit	10X Genomics	120236
Chromium™ i7 Multiplex Kit	10X Genomics	120262
Ab-O Single Cell Sample Multiplexing Kit	BD	633781
BD Single-Cell Multiplexing Kit Library Amplification Component	BD	633782
Stain Buffer (FBS)	BD	554656
Serum Antibody Purification Kit (Protein G)	Abcam	AB128751
Experimental Models: Cell Lines		
H9 hPSCs	WiCell	https://www.wicell.org
H9 SOX2 GFP	WiCell	https://www.wicell.org
XMOO1 iPSCs	Lickert H Lab	https://www.ncbi.nlm.nih.gov/pubmed/29396371
Deposited Data		
Single cell RNA sequencing data	GEO: GSE128357	https://www.ncbi.nlm.nih.gov/geo/query/acc.cgi?acc= GSE128357
Oligonucleotides		
Primers used for qPCR	This study	Table S3
Software		
Cellranger (v3.0.2)	N/A	https://support.10xgenomics.com
CellrangerRkit (v1.1.0)	N/A	https://support.10xgenomics.com
R (v3.3.2)	The R Foundation	https://www.r-project.org
GSEA (v2.2.2)	Subramanian et al., 2005	https://software.broadinstitute.org/gsea/index.jsp
Fiji	Schindelin et al., 2012	https://imagej.net/Fiji
MacroCalcium (Fiji Macro)	N/A	https://gist.github.com/ackman678/5817461

(*Continued on next page*)

Continued

REAGENT or RESOURCE	SOURCE	IDENTIFIER
PhysImage (Fiji Plug-In)	N/A	http://physimage.sourceforge.net/
Imaris	Bitplane	https://imaris.oxinst.com/packages
GraphPad Prism 7	GraphPad	https://www.graphpad.com/scientific-software/prism/
AxIS Navigator	Axion Biosystems	https://www.axionbiosystems.com/products/axis-software
MATLAB	Mathworks	https://de.mathworks.com/products/matlab.html
Other		
U-bottom ultra-low attachment 96-well plate	Corning	7007
Orbital Shaker	Edmund Bühler GmbH	KM CO2-FL

LEAD CONTACT AND MATERIALS AVAILABILITY

Further information and requests for resources and reagents should be directed to and will be fulfilled by the Lead Contact, Mina Gouti (mina.gouti@mdc-berlin.de). This study did not generate new unique reagents.

EXPERIMENTAL MODEL AND SUBJECT DETAILS

Human pluripotent stem cell lines and culture conditions

The female H9, H9 SOX2^{GFP} and the male H1 human embryonic stem cell lines (obtained from WiCell, and approved for use in this project by the Regulatory Authority for the Import and Use of Human Embryonic Stem Cells in the Robert Koch Institute (AZ:3.04.02/0123) and the female XM001 iPSC line (Wang et al., 2018) were maintained in mTESR1 medium (Stem Cell Technologies) on Geltrex LDEV-Free hESC-Qualified Reduced Growth Factor Basement Membrane Matrix (Life Technologies) at 37°C. Cell lines were checked for normal karyotype and were mycoplasma free. The cells were passaged twice a week using Versene solution (Thermo Fisher).

Human samples

Serum from two patients, one male and one female with myasthenia gravis and one healthy male individual, was used with written informed consent from all donors.

METHOD DETAILS

In vitro generation of NMPs from human pluripotent stem cells

Human PSCs were grown for at least three passages and after they reached 70% confluency they were dissociated into single cells using accutase. Single cells were counted using the Countess II automated cell counter (Thermo Fisher) and were plated on p35 dishes coated with geltrex (Life Technologies) at a density of 75.000 - 125.000 / cm^2. The initial plating concentration of the PSCs was adjusted depending on the growth rate of the specific human cell line (XM001: 75.000 / cm^2; H9 line: 110.000 / cm^2; H1 line: 100.000 / cm^2;). The first day the cells were plated in neurobasal (NB) medium supplemented with 10uM Rock inhibitor (Tocris Bioscience), 3uM CHIR99021 (Tocris Bioscience) and 40ng/ml bFGF (Peprotech). NB is a 1:1 medium of Advanced Dulbecco's Modified Eagle Medium F12 supplemented with 1 x N2 (GIBCO), and Neurobasal medium (GIBCO) supplemented with 1 x B27 (GIBCO), 2mM L-glutamine (GIBCO), 40mg/ml BSA fraction V (Sigma), 0.1mM 2-mercaptoethanol (GIBCO). The next day Rock inhibitor was removed and the cells were maintained in NB medium supplemented with 3uM CHIR99021 and 40ng/ml bFGF (Peprotech) until day 3. The medium was changed everyday. At day 3 the cells were analyzed by immunofluorescence for the co-expression of the NMP markers T/BRA and SOX2.

Generation of neuromuscular organoids in 3D

Neuromesodermal progenitors generated from human PSCs were dissociated using accutase to generate a single cell suspension. On day 0 of organoid formation, NMP cells (4,500 – 9,000 / well depending on the cell line) were plated on an ultra-low binding 96-well plate (Corning) in NB medium with 50uM Rho-associated protein kinase ROCK inhibitor (Tocris Bioscience), 10ng/ml bFGF and 2ng/ml IGF1 and 2ng/ml HGF (Peprotech). The plates were centrifuged for 2 min at 350 G. The initial volume in each well was 100ul. At day 2, 50ul of the medium was removed and 100ul of NB medium supplemented with 2ng/ml IGF1 and HGF was added. After day 4 the organoids were maintained in NB medium without the addition of growth factors. On day 10 the organoids were transferred in 60mm dishes (Corning) in 5 mL of medium and after 1 month in 100mm dishes (Corning) with 12 mL NB medium. During the whole period organoids were maintained on an orbital shaker rotating at 75 rpm.

Immunohistochemical analysis of organoids

Organoids were fixed with 4% PFA for 30 minutes to 3 hours (depending on size), washed 3 times in PBS and then left overnight in 30% sucrose solution. Organoids were embedded using a 15% gelatin/10% sucrose solution warmed to 42°C. After letting the gelatine/sucrose harden at 4°C, the resulting blocks were frozen in isopentane and stored in −80°C. Organoids were cryosectioned in 10um thick slices using a MicroM HM 560 Cryostat (Thermo Fisher) and collected on Superfrost Ultraplus glass slides (Thermo Fisher). The gelatin was removed from the slides by incubating them in PBS at 42°C for 20 minutes. Slides were blocked in PBS with 4% Bovine Serum Albumin (BSA) (Sigma Aldrich) and 0.3% Triton X-100 (Sigma Aldrich) for 1 hour at room temperature and incubated with primary antibodies overnight at 4°C. Primary antibodies were washed off 3x with PBS with 0.3% Triton X-100 (PBST). Slides were incubated with secondary antibodies for 1-2 hours at room temperature. After secondary incubation, slides were washed 3x with PBST and mounted using Fluoroshield Mounting Medium with DAPI (Abcam).

Reverse transcription – Quantitative PCR Analysis

Total RNA was isolated from whole organoids or cells growing in monolayer using the RNeasy kit (QIAGEN) according to the manufacturers instructions and digested with DNase I (QIAGEN) to remove genomic DNA. First strand cDNA synthesis was performed with Superscript III system (Invitrogen) using random primers and amplified using Platinum SYBR-Green (Invitrogen). For QPCR the Applied Biosystems Quantstudio 6 Flex Real-Time PCR system was used. PCR primers were designed using NCBI Primer-Blast software, using exon-spanning junctions (Table S3). Expression values for each gene were normalized against GAPDH, using the delta-delta CT method and standard deviations were calculated and plotted using Prism 7 software (GraphPad). Error bars represent standard deviation across three biological replicate samples.

Live imaging of organoids

After plating the single cell suspension in an ultra-low attachment round bottom 96-well plate, the cells were transferred to an Incucyte Zoom (Essen Bioscience) live imaging system. Brightfield pictures were acquired of each well in an interval of 15 minutes with 4X zoom for a period of 5 days. Temperature was maintained at 37°C and CO2 at 5%. Medium changes were performed in between acquisition periods as dictated by the protocol. Images were compressed and exported as an .mp4 movie.

Electron microscopy of organoids

Organoids were fixed with 2% (w/v) paraformaldehyde and 2.5% (v/v) glutaraldehyde in 0.1 M phosphate buffer for 2 hours at room temperature. Samples were postfixed with 1% (v/v) osmium tetroxide, dehydrated in a graded series of ethanol, and embedded in PolyBed® 812 resin (Polysciences, Germany). Ultrathin sections (60-80 nm) were stained with uranyl acetate and lead citrate, and examined at 80 kV with a Zeiss EM 910 electron microscope (Zeiss, Germany). Acquisition was done with a Quemesa CDD camera and the iTEM software (Emsis GmbH, Germany).

Organoids cell dissociation for scRNaseq analysis

Organoids were transferred into a conical tube, washed with PBS and incubated with 1ml accutase (Life technologies) for 10-20mins at 37°C. The organoids were mechanically dissociated using a pipette until a single cell suspension was obtained. The cell suspension was run through a 40 um cell strainer (Miltenyi Biotec) to remove aggregates and debris. A small volume of the cells was used for cell counts and the rest was resuspended in PBS containing 0.04% BSA (Sigma) to give a final concentration of 700 cells/ul.

Tag incubation for single-cell RNA-sequencing analysis

The single cell suspension obtained from organoids was resuspended in 200 uL of BD Stain Buffer (BD Biosciences). Tubes containing the DNA Tags were briefly centrifuged. Each sample (180 uL) was separately transferred to a tube containing a DNA Tag and mixed using a pipette. The mix was left to incubate for 20 minutes at room temperature. Then, 200 uL of BD Stain Buffer was added to the suspension, and the mix was centrifuged for 5 minutes at 300*g*. Supernatant was removed without disturbing the pellet and cells were resuspended in 500 uL Sample Buffer (BD Biosciences). The cells were centrifuged for 5 minutes at 300 g and resuspended in PBS containing 0.04% BSA. The cell suspension was run through a 40 um cell strainer (Miltenyi Biotec) to remove aggregates and debris. A small volume of the cells was used for cell counts and the rest was resuspended in PBS containing 0.04% BSA (Sigma) to give a final concentration of 700 cells/ul.

Single-cell RNA-sequencing

Single-cell transcriptomics profiling derived from day 5 and day 50 3D organoids was done using the Chromium Single Cell Gene Expression system (10X Genomics), according to the manufacturer's recommendations using the Single Cell 3′ Reagent v2/v3 kits (10X Genomics). We confirmed successful library preparation using Bioanalyzer device (DNA HS kit, Agilent) and KAPA Library Quantification (KK4857, Roche). Libraries were sequenced using Illumina HiSeq 4000.

Mapping and extraction of single-cell mRNA transcript counts

Cell Ranger (v3.0.2) was used to perform barcode processing, mapping and UMI (unique molecular identifier) counting and dimension reduction. Reads were aligned to human GRCh38 reference genome and annotated and counted with gene annotations Ensembl version 93. Final results of the Cell Ranger analysis contain the count values of UMIs assigned to each gene in each of

the cells for each respective sample using all mapped reads. The summary of all statistics for each sample and sequencing data discussed in this publication have been deposited in NCBI's Gene Expression Omnibus (Edgar et al., 2002). Data is accessible through GEO Series accession number GSE128357 (https://www.ncbi.nlm.nih.gov/geo/query/acc.cgi?acc= GSE128357).

Single-cell data analysis

Further computational analysis was done using Seurat 3.0.3 (Stuart et al., 2019) filtered feature-barcode matrices. Genes expressed in less than 5 cells and cells with less than 500 features expressed were removed. Top 2000 variable genes were calculated using the variance stabilizing transformation (vst) method. Percent of mitochondrial transcripts were calculated and used for visualization. After data integration using pre-computed anchorsets, cell cycle scores were calculated using cell-cycle genes previously described (Tirosh et al., 2016). Cell cycle scores were used to regress out the cell cycle effects before performing principal component analysis (PCA). After running PCA, uniform manifold approximation and projection (Miller et al., 2006) UMAP dimensional reduction was run to visualize cells. Clusters of cells with similar expression patterns were identified by shared nearest neighbor (SNN) modularity optimization based clustering. Visualizations were done using ggplot2 and rgl (Wickham, 2016; Adler and Kelly, 2019).

Demultiplexing (cell hashing) of cells from samples was done using oligo-tagged antibodies from BD Single-cell Multiplexing Kit following the BD single cell genomics bioinformatics handbook (https://bitbucket.org/CRSwDev/multiplexing_tools). Numbers of UMI-filtered counts for each sample tag were divided by sample tag-specific means. The sample tag with the highest count per cell was selected to classify its sample origin.

We run velocyto.py (La Manno et al., 2018) annotator for each mapped bam file using the default parameters for 10X Genomics technology and the same gtf file for intron-exon annotation. The resulting loom object for each sample was loaded and processed in R using the velocyto.R (v. 0.17) package. We used the UMAP embeddings from Seurat for cell-cell distance calculation and final velocity plots. The estimation of RNA velocity was done with default parameters.

Calcium Imaging of organoids

Calcium imaging was performed on organoid sections. For sectioning, organoids were embedded in low melting point 2% agarose (UltraPure Low Melting Point Agarose, Thermofisher) and slices were obtained using a motorized vibratome (Leica, VT1000 S). Two to three consecutive 200 um section were obtained in iced-cold PBS and immediately transferred to a cell culture insert (Millicell, 0,4 um, 30 mm diameter, Millipore) placed in 6 well plates. Slices were incubated in NB medium containing 1% fetal bovine serum (GIBCO) overnight to allow attachment to the filter before being processed for the calcium imaging experiment.

For calcium imaging experiments 200 uM organoid slices were incubated at 37°C with 4uM of the cell permeant calcium indicator Fluo-8 AM (Abcam) supplement with 0.2% DMSO and 0.05% of cremophor to facilitate dye penetration. After 30 minutes of incubation, tissues were washed two times with culture medium (NB without phenol red), placed in the imaging set up and left to recover for 15 min prior to the start of any optical recording. Samples were continuously perfused with heated (37°C) and oxygenated (Carbogen mix) medium (2 mL/min) during all the experiment.

Fluorescent time series images were acquired with a sCMOS camera (Zyla 4.2 sCMOS, Andor Technology Ltd., Belfast, UK) mounted on an upright microscope (BX51 Olympus, Hamburg, Germany,) using a 10X or 20X water immersion objective and a GFP filter cube set. Images were captured with 100 ms exposure time (10Hz) and bin size 3X3. Camera control and all post hoc calcium imaging analysis were performed using the open source PhysImage package implementing Micro-manager software (Hayes et al., 2018). Fluorescent image stacks were processed using ''Calmager'' filter to obtain a $\Delta F/F$ file. A standard-deviation image was generated in order to detect pixels displaying the most variable intensity during the recording. Individual or small cell clusters were automatically identified and the $\Delta F/F$ variation over time was plotted for the defined regions of interest. Finally, a cycle trigger average (CTA) was performed to identify cell morphology. In preliminary 2D culture set of experiment we observed that Fluo-8 AM dye was preferentially uptaken by the neuronal population but not myofibers, offering us an adequate method to investigate neural activity.

Contraction analysis

Video segments of equal length were recorded using a brightfield microscope (DMI1, Leica) in 3 different regions of the same organoid using 20X zoom. To quantify muscle contractions, each movie was analyzed separately where each visible contraction was counted and then averaged for the whole organoid.

To analyze and map organoid muscular contraction, bright field time series images were automatically thresholded using ImageJ software to identify organoid border. A binary stack was created and contractile regions were visually identified. Regions of interest were defined and variations of organoid area (in pixel), used as a proxy of physical contraction, were plotted over the time series.

Cell counting and statistical analysis

To quantify the percentage of neurons and muscle in the organoids, TUJ1 expression was used as a neural marker and Myosin Skeletal Fast (MSF) as a marker of skeletal muscle. In z stacks generated by immunofluorescence analysis, the $TUJ1^+$ and MSF^+ areas were measured separately using ImageJ by defining polygon areas and then normalized to the total area of the organoid sections.

To quantify the percentage of $ChAT^+$, $GFAP^+$ and $SMI32^+$ areas in organoid sections, immunofluorescence z stacks were used and normalized to the total area of the organoids.

To determine and quantify the number of AChR clusters in sections of organoids, α-bungarotoxin staining was performed. Sections of organoids previously fixed were incubated with Alexa Fluor 647 conjugated α-bungarotoxin (Thermo Fisher) for 2 hours to label AChRs. Images were acquired with 80X zoom in 3 random locations per sample (n = 3-16). The generated stacks were analyzed using ImageJ's Particle Analyzer. Clusters smaller than 5 μm^2 were excluded from analysis. To assess cluster number, AChR clusters were quantified for each image and then normalized to the number of Myosin Skeletal Fast positive fibers present in the quantified image.

To determine the number of co-localizing cells, stacks acquired with 20X zoom of whole organoid sections were analyzed using Imaris (Bitplane). Each channel was quantified separately. Particles with a diameter of less than 7 μm were excluded from the analysis. Co-localized cells were manually counted and compared to the software analysis. Positive cells were then normalized to the total number of $DAPI^+$ cells in the whole section.

Microelectrode array (MEA) recording and analysis

Whole organoids kept in neurobasal medium were transferred prior to recording to a 6-well MEA plate (M384-tMEA-6W, 64 electrodes, 11.5 μm diameter, 300 μm spacing, Axion Biosystems) and recorded in a Maestro Pro MEA system (Axion Biosystems). Media was removed from each well until only a thin layer remained to promote attachment of organoids to the electrode grid. Temperature was maintained at 37°C and CO2 at 5%. During some recordings, 50 μM Glutamate or 10 μM ACh or 50 μM NMDA + 40 μM 5-HT (Sigma Aldrich) were added in warm media to stimulate organoid activity. To record inhibitory pharmacologic effects on organoids, 10 μM Curare or 50 μM APV and 40 μM CNQX (Sigma Aldrich) or 1 μM Tetrodotoxin (Abcam) were added to the medium. After inhibitory recordings the organoids were washed with warm basal medium and left to stabilize for 30 minutes, after which a new recording was performed. The signal was sampled at 25 kHZ and stored using the AXIS Navigator Software (Axion Biosystems). Data was exported as .csv files for analysis. A threshold 6 times the standard deviation above the background noise was used to detect extracellular spikes in each channel with a 2 ms refractory period imposed after each detected spike. Connectivity between electrodes was determined within a time window of 40 ms. Analysis of the resulting connectivity data was performed using a MATLAB script where all spikes were counted for each single electrode and a combinatorial non-repetitive description of each paired electrode connections was obtained and plotted.

Myasthenia gravis disease modeling

Serum from two patients diagnosed with Anti-AChR MG having high antibody titters (Patient 1 > 20; Patient 2 = 7.6) was collected and IgG fractions were purified using a Protein G Serum Antibody Purification Kit (Abcam) according to the manufacturers instructions.

Purified IgG was reconstituted using the Kit Elution Buffer and IgG content was quantified using a Nanodrop 1000 spectrophotometer (Thermo Fisher). Contracting NMOs were incubated with MG patient IgGs (300 nM final concentration) supplemented with 2% human serum for 3 days. IgGs from healthy human serum (Sigma) was used as a control. The medium was changed every day, and after 3 days of treatment, the NMOs were collected for fixation and immunofluorescence analysis. Analysis of the contractile activity of at least 3 different NMOs was performed before and after treatment (3 days) with specific IgGs. Video segments of 5 minutes in length were recorded using a Leica SP8 confocal, and exported as .avi files. 3 different close-up areas of each NMO were recorded and averaged. Number of muscle contractions were obtained by isolating one visually recognizable contractile area of the video recording using ImageJ (as described previously). The number of peaks resulting from area displacement during contraction were counted and averaged.

QUANTIFICATION AND STATISTICAL ANALYSIS

Data are reported as the mean ± standard deviation, using a significance level of $p < 0.05$. The number of replicates is indicated in the figure legends or in Table S1; "N" denotes the number of independent experiments and "n" denotes the number of organoids, as appropriate. Data were analyzed by one-way and two-way ANOVA, using Bonferroni test for multiple comparisons and Welch's t test for pairwise comparisons (Prism 5-7, GraphPad).

DATA AND CODE AVAILABILITY

The single cell data have been deposited in the gene expression omnibus (GEO) under ID code GEO: GSE128357 (https://www.ncbi.nlm.nih.gov/geo/query/acc.cgi?acc= GSE128357). The MATLAB code for MEA analysis is available from the Lead Contact on request.